Redox conditions across the Upper Cambrian in

Western Newfoundland, Canada.

By

Miracle-Mary Chisom Okafor

A thesis submitted to the School of Graduate Studies

In partial fulfilment of the requirements for the degree of

Master of Science

Department of Earth Sciences

Memorial University of Newfoundland

St. John's, Newfoundland.

February 2023.

ABSTRACT

The lower part of the Martin Point section (~ 110 m - rhythmites) spans the uppermost Shallow Bay and lowermost Green Point formations (uppermost Franconian–lowermost Trempealeauan) of the Cow Head Group (western Newfoundland, Canada). It records two post-SPICE events (SPICE – Steptoean Positive Carbon Isotope Excursion) marked by negative $\delta^{13}C_{carb}$ excursions (NL1 and NL2) that were also documented in South China. The petrographic and chemical screening of the investigated carbonate samples proves the preservation of at least near-primary geochemical signatures. The proxies of weathering (e.g., Mn, Fe, Al, and $\sum REE$), bioproductivity (e.g., $\delta^{13}C_{org}$, TOC, P, Ni, Zn, and Cu), and paleoredox (e.g., Cr, Th/U, Ce/Ce*) have been utilized to reconstruct the paleoenvironmental conditions during the post-SPICE events. The TOC, P, Ni, Cu, Cr, $\sum REE$, Mn, Fe, and U enrichment-factor profiles exhibit a positive pulse at the base of NL2 (upper negative $\delta^{13}C_{carb}$ excursion), followed by a drop. This might have resulted from shoaling organic-rich anoxic waters into an oxygenated shallow environment during transgression, which led to a negative shift in the $\delta^{13}C_{carb}$ and a decrease in TOC contents as well as an increase in the $\delta^{13}C_{org}$. The correlated enrichment in Zn and $\delta^{15}N_{org}$ values and the Ce/Ce* around unity are consistent with the shoaling scenario. A similar scenario seems to be consistent with NL1 (lower negative $\delta^{13}C_{carb}$ excursion) although the lower resolution of correlated proxy variations makes the interpretations based on a few points and to be therefore taken with caution.

The upper part of the Martin Point section spans the upper Martin Point Member (upper Furongian, ~90 m) of the Green Point Formation of the Cow Head

Group. It records the HERB event (HERB - Hellnmaria-Red Tops Boundary) marked by a negative $\delta^{13}C_{carb}$ excursion at the base of the *Econodontus notchpakensis* conodont Zone. The HERB paleoenvironmental proxy enrichment profiles exhibit comparable patterns to those of the post-SPICE, which suggests that the HERB event started with a similar scenario of transgression and shoaling of organic-rich anoxic water into the water settings. However, the TOC profile shows a small gradual enrichment (~1 %), above the peak of the excursion, correlated with a broad negative $\delta^{13}C_{org}$ shift (~2 ‰), and a positive Al/Ti shift. This may suggest possible minor interruptions by sealevel drop and/or an episode/pulse of enhanced wind-blown inputs of weathered terrigenous material.

ACKNOWLEDGEMENTS

TABLE OF CONTENTS

LIST OF FIGURES

LIST OF TABLES

LIST OF APPENDICES

Appendix 1. Samples, isotopic and elemental compositions of the investigated

carbonates (concentrations of elements are in ppm). The $\delta^{13}C_{carb}$ and

$\delta^{18}O$ data of the post-SPICE interval are from Azmy (2019b) whereas

the entire HERB data (elemental and isotopic geochemistry) are from

Wang and Azmy (2020).

CO-AUTHORSHIP STATEMENT

The thesis is constructed in a manuscript format and consisting of six chapters. It has been submitted (Sections 5.1 and 5.2) to and accepted (pending review) by the Journal of Marine and Petroleum Geology. Reviewed manuscript has been resubmitted to the journal and the reviewers' comments have been already considered in the current thesis manuscript.

Prof. Karem Azmy designed the mainframe for the research study of the thesis. As the primary author, I was responsible for aspects of the research project, reviewing the literature, performing the laboratory work, analyzing and interpreting the data, and preparing the manuscript. Meanwhile, the co-author (Prof. Karem Azmy) guided the research progress, offered advice for interpreting the data and corrected the manuscripts before submission.

CHAPTER I

INTRODUCTION AND OVERVIEW

Well-preserved carbonates usually retain primary/near primary isotope and elemental geochemical signatures of proxies that are very useful for the reconstruction of paleoenvironmental conditions during the geologic past (e.g., Wignall and Twitchett, 1996; Veizer et al., 1999; Algeo and Maynard, 2004; Kimura et al., 2005; Whalen and Day, 2008; Śliwiński et al., 2010; Tripathy et al., 2014; Acharya et al., 2015; Yao et al., 2017, Zhang et al., 2022, Yang et al., 2023). The Upper Cambrian-Lower Ordovician slope carbonates of the Martin Point section are widely exposed in western Newfoundland (Canada) and are among the best-preserved Upper Cambrian marine carbonates on the eastern Laurentian margin. The succession is generally well defined in terms of its sedimentology, lithostratigraphy, biostratigraphy (e.g., James and Stevens, 1986), and chemostratigraphy (e.g., Azmy, 2019a; 2019b; Wang and Azmy, 2020).

During the Late Cambrian, the sealevel changes influenced not only the redox conditions and primary productivity (e.g., Landing, 2012; 2013; Terfelt et al., 2012; Terfelt et al., 2014; Azmy et al., 2015) but also the chemistry of seawater such as the contents of P, Al, Ni, Cu, Si, REE (Rare Earth Elements), Th, U, Fe, and Mn (e.g., Wignall and Twitchett, 1996; Wignall et al., 2007; Arnaboldi and Meyers, 2007; Dahl et al., 2010; Voegelin et al., 2010; Brennecka et al., 2011; Dickson and Cohen, 2012; Romaniello et al., 2013). Trace element proxies were found to reflect changes in climate (dry vs. wet) expressed in riverine inputs of detrital weathered material (e.g., Al, Si, and REE), bioproductivity (Ni, Zn, and Cu), and oceanic bottom water redox

conditions (Mo, U, V, Th, Fe, and Mn; Wignall and Twitchett, 1996; Wignall et al., 2007; Śliwiński et al., 2010; Dickson and Cohen, 2012; Acharya et al., 2015; Tessin et al., 2019; Abshire et al., 2020; Yano et al., 2020; Wang and Azmy, 2020; Bian et al., 2021).

Sealevel changes may influence oxidation of organic matter in seawater, thus resulting in variations in the total organic content (TOC), $\delta^{13}C$ of carbonates, and C- and N-isotope compositions ($\delta^{13}C_{org}$ and $\delta^{15}N_{org}$) of the organic matter (e.g., Quan et al., 2008; Kump et al., 2011; Wang and Azmy, 2020). Marine redox changes can also play a vital role in controlling the oxidation of organic matter through biogeochemical cycling of redox sensitive elements and ratios (e.g., Fe, Mn, U, V and Th/U; Zhao et al., 2020).

Global Steptoean Positive Carbon Isotope Excursion (SPICE) is a distinct chemostratigraphic feature in lower Paleozoic rocks and is preceded in some cases by pre-SPICE negative shift (Schiffbauer et al., 2017; Pulsipher et al., 2020). The immediate top of the SPICE positive excursion might inflect into a negative C-isotope shift in some places and has other similar overlying post-SPICE shifts such as those shown by the $\delta^{13}C_{carb}$ profiles of the Wa'ergang section in South China and Martin point section in western Newfoundland (Li et al., 2017; Azmy 2019b). The investigated Martin point section records the post-SPICE negative shifts of NL1 (correlated possibly with the lower boundary of Stage 10; Li et al., 2017; Azmy 2019b) and the overlying NL2 (Azmy 2019b). Earlier studies suggest that the SPICE represents a widespread ocean anoxic/euxinic event resulting in the preservation of

organic matter (C_{org}) and pyrite (Gill et al., 2011). The oxygen level was very low and increased relatively at the end of the event (Elrick et al., 2011).

This study is among the very few to investigate the variations in the elemental paleoproxies retained in the carbonates spanning the Late Cambrian. The main objectives of the current study are to evaluate the degree of preservation of the geochemical signatures of the paleoenvironmental proxies in the Martin Point carbonates, to better understand the influence of climate and sealevel changes on the chemistry of the Late Cambrian seawater and to investigate the paleo-seawater redox conditions that dominated after the end of the SPICE event.

CHAPTER II

GEOLOGIC SETTING AND STRATIGRAPHIC FRAMEWORK

2.1 Geologic settings

Western Newfoundland is located on the eastern (paleosouth) Laurentian margin that retains the best-preserved Paleozoic sedimentary successions and constitutes an extension of the Appalachian Mountain and a part of the Humber zone (Williams, 1978; Cooper et al., 2011), where these sediments span the Cambrian to Silurian and rest unconformably on the Grenvillian basement. The Laurentian plate developed by active rifting of Rodinia around 570–550 Ma that resulted in the opening of the Iapetus Ocean (e.g., Cawood et al., 2001; Hibbard et al., 2007) and a pre-platform shelf formed and was eventually covered by clastic sediments (Williams and Hiscott, 1987; James et al., 1989). During the Late Cambrian, major subsidence led to marine transgression and deposition of thick carbonate deposits on the Laurentian platform margin that part of which swept off the shelf to form the slope carbonates of the Cow Head Group (Fig.1; Wilson et al., 1992; Cooper et al., 2001; Landing, 2007; 2012; Lavoie et al., 2012).

The synrift successions in western Newfoundland consist of the Labrador Group deposits that include the Bateau, Lighthouse Cove, and Bradore formations, where the Bradore Formation sediments show the transition to passive margin and deposition of the Middle to Late Cambrian high energy carbonate platform of Port au Port Group (Cawood et al., 2001; Allen et al., 2001). This was followed by the deposition of the overlying low-energy carbonates of the Lower Ordovician St. George Group (Stenzel et al., 1990).
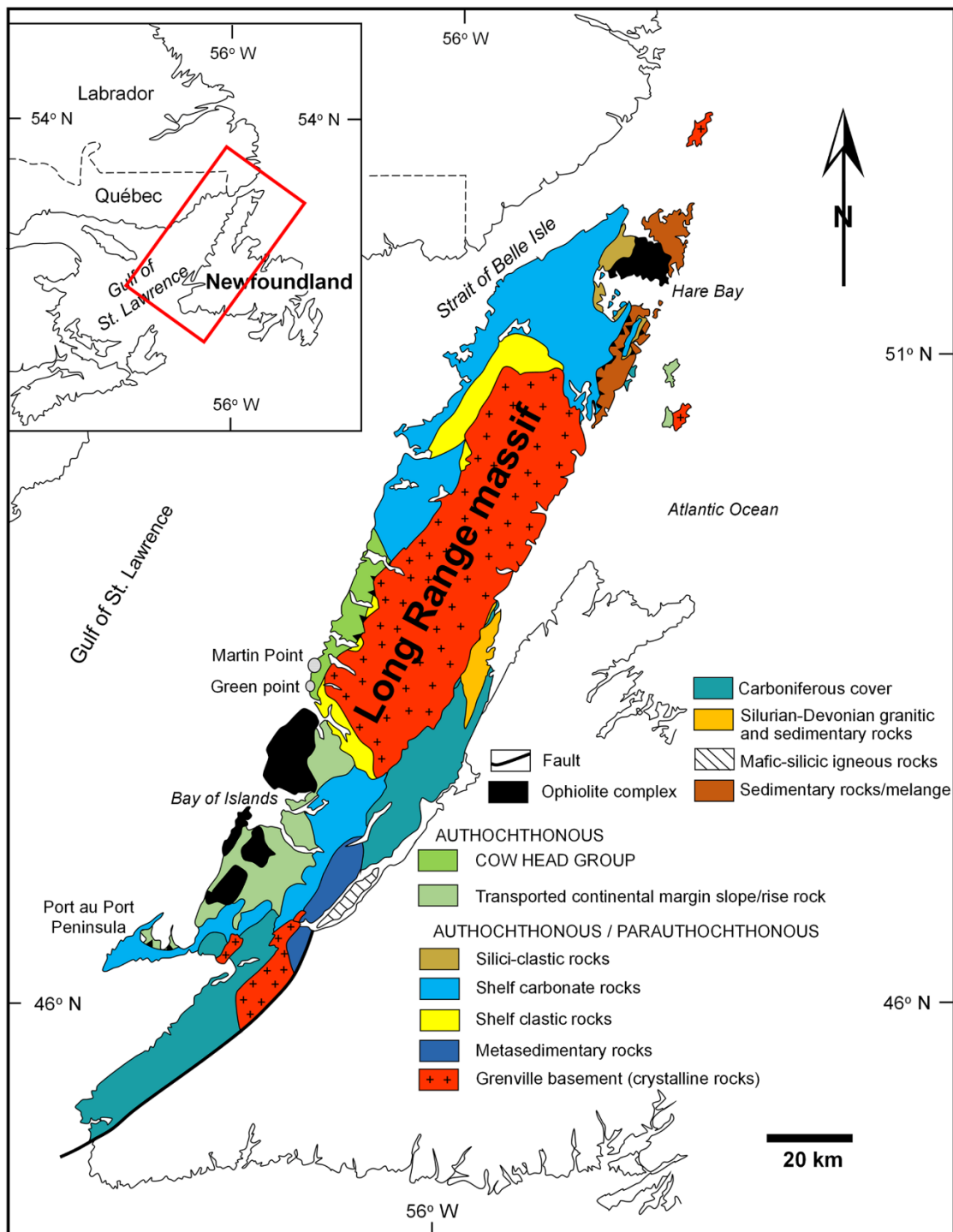
Fig. 1. Map of the study area illustrating the surface geology and location of the Martin Point section (49°40' 51" N, 57°57' 36" W) in Western Newfoundland, Canada (adapted from James and Stevens, 1986; Cooper, et al., 2001)

The Curling and Cow Head groups constitute the allochthonous Middle Cambrian to Middle Ordovician sedimentary succession of the Humber Arm Supergroup (Kindle and Whittington, 1958). The Cow Head Group was deposited along the southeast-dipping slope as debris reworked from the shallow water carbonates and transported to deeper water settings to constitute an apron including the Shallow Bay and Green Point formations.

2.2 Lithostratigraphy

The Cow Head Group comprises a 300–500 m-thick succession of sedimentary rocks (James and Stevens 1986) characterized by conglomerate beds intercalated with deep-water carbonates, quartz-rich, coarse-grained limestones, and minor siliciclastic facies. It is deemed to represent deposition on a continental slope adjacent to a Middle Cambrian to Middle Ordovician carbonate bank (Hiscott and James, 1985; James and Stevens, 1986) and became relatively steeper during the Arenig (Hiscott and James, 1985). This is consistent with the occurrence of large blocks of shallow water limestone in mega conglomerates interbedded with deep-water limestone, shale, and siltstone (Mcllreath and James, 1978; James and Mountjoy, 1983; Coniglio and James, 1985). The paleographic settings of the Cow Head Group are such that, toward the southeast, some fine-grained shaly limy mudrocks are predominant, which constitute the Green Point Formation, while on the northwest, the lithologies grades sharply into coarse-grained facies referred to as the Shallow Bay Formation (James and Stevens, 1986). The Green Point Formation consists of lenticular and continuous conglomeratic carbonates incorporated with distal fine-grained carbonates mixed with siliciclastic hemipelagic facies making up

the allochthonous sequence of the Cow Head Group (James and Stevens, 1986).

Rocks of the Cow Head Group are capped conformably by an over 1700 m thick

green sandstone flysch named the Lower Head Formation. Above this formation lies a

contact with archives of episodic tectonic events (Blamey et al., 2016).

The Green Point Formation comprises three members. The basal unit is the

Martin Point Member, which is composed of green and black shale, minor red shales,

limestone ribbons, calcareous sandstones and siltstones. It is about 100-150 m thick

and dated to be Late Cambrian based on its faunal and floral contents. The Overlying

Broom Point Member is about 80 m thick and composed of ribbon to parted

limestone. It is dated Early Canadian or Tremadoc. Above the parted limestone

sequence lies the St. Paul's member, a twin member of the Martin point composed of

green, black and distinctively red shales with some variable beds of limestone,

siltstones and dolomites. Capping the entire succession are carbonates and

siliciclastics of upper Canadian or lower White Rock and uppermost Arenig (James

and Stevens, 1986).

The Martin Point member is exposed at the lower Martin Point section and is a

part of the Green Point Formation of the Cow Head Group (Fig. 2). It consists of

green and black shaley mudstones with thin beds of lime mudstone, siltstone, and

ribbon limestone. The member is interpreted to occupy a more distal position on the

continental rise than that of equivalent strata outcropping at Broom Point on the Cow

Head Peninsula and Lower Head and occupying the toe of the slope (James and

Stevens, 1986). Bedded carbonates and siliciclastics are more abundant volumetrically

than the lime conglomerates in this section, with siliciclastics being the dominant

lithology in the Arenig at Martin Point. Minimal undercutting of bedded strata by conglomerates was observed at these localities. In more proximal localities undercutting by conglomerates can be quite pronounced. The predominance of argillites in the Arenig portion of the Martin Point section plus the red shales reflects well-oxygenated bottom waters and suggests deposition more distally on the continental rise.

The investigated interval (~ 110 m) of the lower Martin Point section (Fig. 1) spans the uppermost part of the shallow Bay Formation (upper Tuckers Cove member) and the lowermost part of the Green Point Formation (lower Martin Point Member) of the Cow Head Group (Fig. 2). The lithostratigraphy of the section has been studied and discussed extensively by James and Stevens (1986) and it is therefore only summarized here.

The section consists of dark grey to black fissile shale alternating with thin (~ 1 cm thick) interbeds of ribbon limestone rhythmites. Siltstone interbeds (up to 1 cm thick) may occasionally co-occur with shale but are not abundant. The limestone interbeds (rhythmites) vary from isolated and thin to up to 20 cm thick. Carbonate conglomerate/breccia beds may occur and contain clasts (up to 25 cm) of shallow-water carbonates that were transported into deep-water facies along the slope of the Laurentian margin (James and Stevens, 1986).
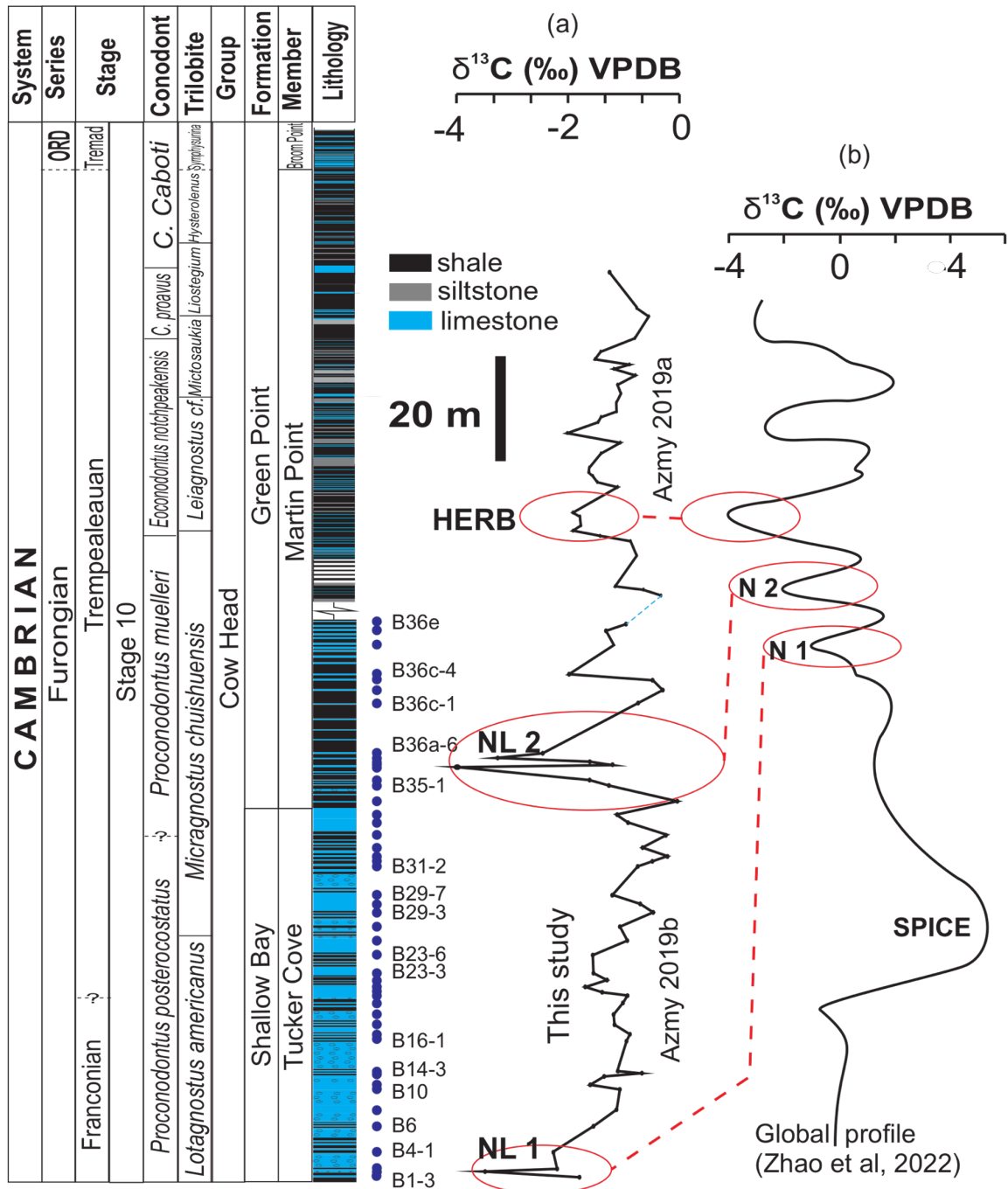
Fig. 2. (a) Stratigraphic framework and C-isotope profile of the investigated lower Martin Point section in western Newfoundland, Canada (after Azmy, 2019b) illustrating bed number and detailed measured positions of investigated samples. The Conodont *(P. muelleri and P. posterocostatus)* and trilobite zones zones have not been documented yet in the Martin Point section but are based on the global scheme (e.g., Li et al., 2017) and that suggested for the Cow Head Group and North America (Barnes, 1988; Miller et al., 2011). The HERB C-isotope profile is from Azmy (2019a). (b) The global C-isotope profile of the Upper Cambrian (after Zhao et al., 2022) with the correlated post-SPICE negative δ^{13}C shifts (N1 and N2) of the Wa'ergang section (Li et al., 2017) marked on.

2.3 Biostratigraphy

The faunal occurrences in the Martin Point section are limited compared with their counterparts of the same age in other sections (Azmy, 2019a,b). The conodont biozonation in the studied interval at Martin Point (Fig. 2a) spans approximately the lower part of the *Proconodontus muelleri* and continues down to the underlying *Proconodontus posterocostatus* on the global conodont biozonation scheme, including that of N. America (James and Stevens, 1986; Barnes, 1988; Miller et al., 2011; Li et al., 2017). In the Lawson Cove and Sneakover Pass section of Utah (USA), the *Proconodontus muelleri* and the *Proconodontus posterocostatus* have been documented below the *Econodontus notchpekensis* (Miller et al., 2011), where the base of the *notchpekensis* is marked by the distinct global HERB (Helenmaria – Red Tops Boundary) $\delta^{13}C$ excursion (Miller et al., 2011; Li et al., 2017; Azmy, 2019a). The HERB $\delta^{13}C$ has been recorded by the C-isotope profile of the GSSP section of Green Point (e.g., Miller et al., 2011) and that of the Martin Point (Azmy, 2019a) at a stratigraphic level above the currently investigated interval (Fig. 2a). However, the *P. muelleri* and *P. posterocostatus* zones have not been documented yet in the Martin Point section but based on the global biozonation scheme and C-isotope stratigraphy, have been suggested by an earlier study (Azmy 2019b) to be expected at a stratigraphic level correlated with that of the currently studied interval (Fig. 2). The lower part of the Cambrian Stage 10 spans the *P. postercostatus* and P. *muelleri* conodont zones (Fig. 2; Li et al., 2017). The base of Stage 10 has been suggested to be marked by a negative $\delta^{13}C$ excursion (N1) recorded by the C-isotope profile of the Wa'ergang section in South China (Li et al., 2017 their figure 2; Li et al., 2018),

which is also correlated with a counterpart (NL1) recorded by the Martin Point C-isotope profile (Fig. 2b; Azmy, 2019b).

No elaborate trilobite biozonation scheme has been constructed for the Martin Point section. However, Agnostid trilobites are distributed globally in the upper Cambrian to lower Ordovician sections and are used conveniently for correlations on the same continent and beyond (Saltzman, et al., 2000). The Martin Point interval spans the uppermost Franconian and the lowermost Trempealeauan, which places the interval considerably below the *lotagnostus americanus* trilobite zone (Cooper et al., 2001). However, Landing, et al (2010; 2011) and Westrop (2011) disagree as they limit this zone to its topotype in Quebec, hence not fitting for defining a global time-stratigraphy unit. The exact position of the trilobites has been difficult to determine since no diagnostic trilobites have been documented for this section. A well detailed trilobite zonation scheme has been documented in the correlated Wa'ergang section of southeast China (Li et al., 2017). The section began well below the base of stage 10 and has the potential to define the base of this stage (Peng et al., 2014; Li et al., 2017). The two post-SPICE negative δ^{13}C excursions (NL1 and NL2) and the overlying HERB event correlate to the N1, N2 and N3 negative excursions, respectively, of Li et al. (2017). This correlation argues for strong reliability on their already established trilobite zonation (e.g., Li et al., 2017), through which a similar trilobite zonation can be constructed for the Martin Point section. Therefore, the trilobite Zones of the Martin Point section consist of, in upward profiling, the *Lotagnostus americanus* zone, *Micragnostus chuishuensis* zone, *Leiagnostus Cf. bexelli-Archaeuloma taoyuanense* zone, *Mictosaukia Striata-Fatocephalus* zone, *Leiostegium constrictum-Shejiawania brevis* zone, *Hysterolenus* zone and

the *Symphysurina* zone (Fig. 2). The NL-1 corresponds to the base of the *Lotagnostus americanus* zone suggesting the existence of the base of Stage 10 at Martin Point section. The NL-2 correlates to the *Micragnostus chuishuensis* zone and the HERB lies just above the *Leiagonostus cf. bexelli-Archaeuloma taoyuanense* zone, while the Cambro-Ordovician boundary is identified at the base of the *Symphysurina* zone (Fig. 2).

CHAPTER III

MATERIALS AND METHODOLOGY

3.1 Sample preparation

A total number of fifty samples (Appendix 1) were collected at close intervals from the lower parts of the Martin Point section (49° 40' 51" N, 57° 57' 36" W; Fig. 2) in western Newfoundland, Canada (Fig. 1; James and Stevens, 1986; Cooper et al., 2001). Samples were retrieved from the laminated lime mudstone interbeds to avoid allochthonous clasts. Thin sections were cut and stained with Alizarin-Red-S and Potassium ferricyanide solutions (Dickson, 1966) for petrographic examination by a polarizing microscope and evaluation of diagenetic alteration (recrystallization) and abundance of pyrite and siderite. They were also examined by a Technosyn 8200 MKII cold cathodoluminoscope, which was operated at 0.7 mA current and 8kV accelerating voltage.

A mirror-image slab of each thin section was prepared and polished for microsampling. The slabs were cleaned in an ultrasonic bath, washed with deionized water, and dried overnight at 50°C prior to microsampling for geochemical analyses. Powder samples were extracted from micrites free of secondary calcite or other diagenetic phases (e.g., cement veinlets) using a low-speed microdrill under a binocular microscope.

3.2 Isotopic analysis

For total organic carbon (TOC) and organic C- and N-isotope analyses, ~ 0.5 g of powder sample was placed in a 50 ml-Nalgene centrifuge tube and dissolved in

20% (v/v) HCl repetitively to remove carbonates following the methodology of Vindušková et al. (2019). In addition, no oil residues or bitumen was observed during acid digestion. The remaining residue was separated by centrifugation and decantation and washed with deionized water at least three times before drying overnight at ~40°C. The $\delta^{13}C_{org}$ values of isolated organic matter were measured by a Carlo Erba Elemental Analyser (EA) coupled with a Thermo Finnigan DELTA V plus at the isotope laboratory of Memorial University of Newfoundland. The uncertainty calculated from repeated measurements of standards was ~0.2‰. The TOC value was calculated from the peak area of the individual analyses based on mass. The results (σ < 0.25) were calibrated to the standards L-glutamic acid ($\delta^{13}C_{VPDB}$ = −26.74 ± 0.06‰ VPDB), Suprapur $CaCO_3$ ($\delta^{13}C_{VPDB}$ = −40.11 ± 0.15‰ VPDB), SPEX $CaCO_3$ ($\delta^{13}C_{VPDB}$ = −21.02 ± 0.10‰ VPDB), and B2153 low org soil ($\delta^{13}C_{VPDB}$ = −26.71 ± 0.24‰ VPDB). The $\delta^{15}N_{org}$ values were measured by VARIO ISOTOPE CUBE (ELEMENTAR) connected to a Thermo Finnigan DELTA V plus isotope ratio mass spectrometer at the isotope laboratory of Memorial University of Newfoundland. The results (σ < 0.15) were calibrated to the standards IAEA-N-1 ($\delta^{15}N_{air}$ = 0.43 ± 0.07‰ air), IAEA-N2 ($\delta^{15}N_{air}$ = 20.32 ± 0.09‰ air), and B2151 high-organic sediment ($\delta^{15}N_{air}$ = 4.35 ± 0.20‰ air).

3.3 Elemental analysis

For elemental analysis, 10 mg of powder sample was digested in 2% (v/v) pure HNO_3 for 70–80 min and analyzed for major and trace elements, including rare earth elements (REEs), using an Agilent 8800 triple quadrupole inductively coupled plasma mass spectrometer (ICP-MS). The relative uncertainties of the measured element

values are better than 5% based on repeated analyses of standards (SBC-1-SY and SGR-1b-SY). Although Ce anomaly (Ce/Ce*) is usually calculated conventionally based on the equation $[(Ce/Ce*)_{SN} = Ce_{SN}/(0.5La_{SN} + 0.5Pr_{SN})]$ (Bau and Dulski, 1996), La was found to behave in an anomalous way that might overvalue the Ce anomaly pattern (Tostevin et al., 2016). An alternative more appropriate equation $[(Ce/Ce*)_{SN} = Ce_{SN}/(Pr_{SN}^2 / Nd_{SN})]$ independent of La, suggested by Lawrence et al. (2006), was therefore used for the current study.

The enrichment factor values of the paleoenvironmental proxies were utilized to minimize the influence of contributions from siliciclastic inclusions, in case they occur, since the investigated carbonates occurred in rhythmites (alternating lime mudstones and shale interbeds). The enrichment factor was calculated using the equation (Tribovillard et al., 2006): $X_{EF} = [(X/Al)_{Sample} / (X/Al)_{PAAS}]$ where X is the proxy element and X and Al values (in ppm) are normalized to post-Archean average shale (PAAS; Taylor and McLennan, 1985; McLennan, 1989; Tribovillard et al., 2006; Ansari et al., 2022).

CHAPTER IV

RESULTS

Petrographic examinations indicated that the examined Upper Cambrian carbonates of the lower Martin Point section are dominantly micritic (<4 μm) to near micritic (~10 μm) lime mudstones to rarely peloidal lime mudstones that exhibit dull to non-luminescence under the cathodoluminoscope (Fig. 3a and b; Azmy, 2019b). Pyrite is rare (ca. <1 %) and no siderite was observed.
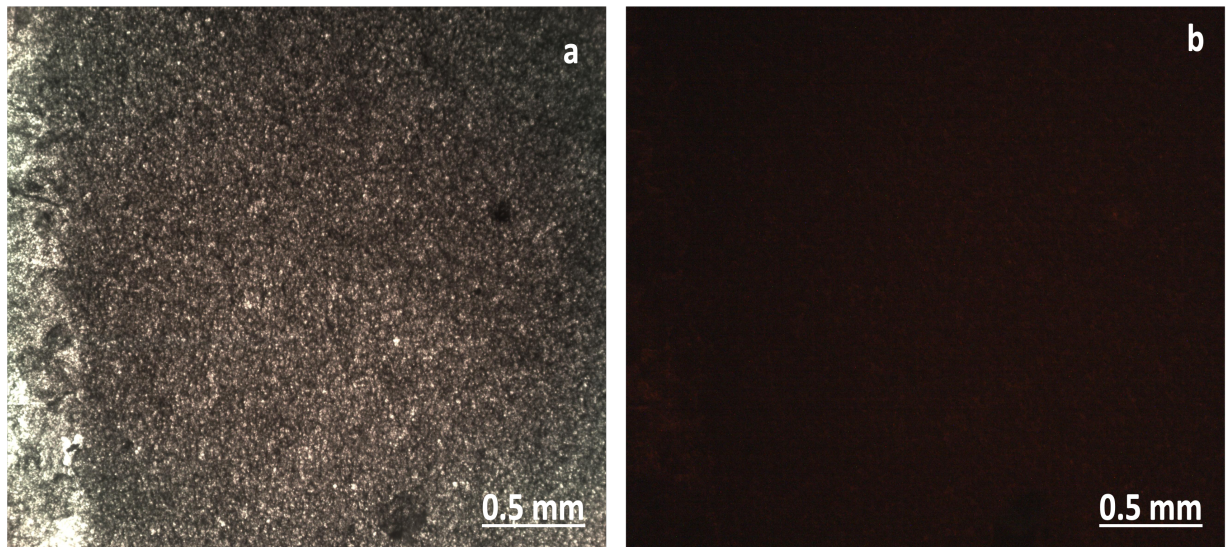
Fig. 3. Photomicrographs of the investigated carbonates showing (a) micritic lime mudstones with fracture-filling cement to the left (Crossed polars; Sample B4-1) and (b) CL image of (a).

Table 1: Summary of statistics of isotopic and trace element geochemical compositions of the Upper Cambrian carbonates of Martin Point section. HERB data are from Wang and Azmy (2020).

	$\delta^{13}C_{carb}$ ‰ (VPDB)	$\delta^{18}O$ ‰ (VPDB)	$\delta^{13}C_{org}$ ‰ (VPDB)	TOC Wt.%	$\delta^{15}N_{org}$ ‰ (Air)	Sr (ppm)	P (ppm)	Ni (ppm)	Cu (ppm)	Zn (ppm)	Rb/Sr	Cu/Sr	Cr (ppm)	Al/Ti	∑REE (ppm)	Mn (ppm)	Fe (ppm)	U (ppm)	Th/U	Ce/Ce*
HERB																				
n	48	48	36	37	21	17	17	17	17	11	17	17	17	17	17	17	17	17	17	17
Mean	-0.6	-7.1	-29.1	1.0	3.0	356	142	4.1	7.6	6.2	0.010	0.028	4.8	38	49	380	2542	1.1	1.4	0.8
Stdev	0.8	0.3	0.7	0.6	1.0	226	45	1.9	3.1	7.6	0.006	0.019	1.3	14	22	142	1876	1.0	1.5	0.1
Max	1.0	-6.4	-27.8	3.1	5.0	980	252	8.5	17.4	21.7	0.023	0.090	6.9	80	95	572	6900	3.6	5.1	1.0
Min	-2.1	-7.8	-30.5	0.3	0.8	165	85	1.9	4.7	0.6	0.002	0.009	2.8	19	25	150	785	0.2	0.1	0.7
POST-SPICE																				
n	49	49	32	28	29	32	32	32	32	32	32	32	32	32	32	30	32	32	32	32
Mean	-0.9	-7.4	-28.9	0.7	3.1	308	145	1	0.7	2.1	0.004	0.003	1.3	6	54	291	1673	0.8	1.5	1.1
Stdev	1.2	0.5	1.6	0.6	1.4	224	75	0.8	1.2	1.9	0.003	0.003	0.6	5	27	154	1714	0.9	1.5	0.1
Max	1.0	-5.3	-25.3	3.0	5.2	1,294	391	4.7	5.4	11.2	0.013	0.014	2.8	29	122	802	7007	4.7	7.8	1.4
Min	-5.0	-8.2	-32.5	0.1	-0.7	73	38	0.1	0.0	0.4	0.000	0.000	0.3	1	13	91	397	0.1	0.1	0.9

The total organic content (TOC; 0.72 ± 0.64 wt.%) values range from 0.10 to

2.98 wt.% and exhibit a weak correlation with their $\delta^{13}C_{org}$ values (-28.9 ± 1.6‰

VPDB) and moderate correlation with their $\delta^{15}N_{org}$ (3.1 ± 1.4‰ air) counterparts (R^2

= 0.22 and 0.44, respectively; Fig. 4a and b; Appendix 1; Table 1). The mean TOC,

$\delta^{13}C_{org}$, and $\delta^{15}N_{org}$ values of the investigated samples seem to be similar to those

documented for the overlying younger carbonates of the HERB event (1.0 ± 0.6%; $-$

29.1 ± 0.7‰ VPDB; and 3.0 ± 1.0‰ air, respectively; Appendix 1; Table 1; Wang

and Azmy, 2020). The mean $\delta^{15}N_{org}$ value is generally close to that of present-day

Black Sea sediments (2.5‰ to 3.6‰; Çoban - Yıldız et al., 2006; Fry et al., 1991)

although signatures from the Martin Point section have a wider spread.

An earlier study of C-isotope stratigraphy of the currently investigated interval

of the Martin Point section (Azmy, 2019b) documented two distinct (NL1 and NL2)

post-SPICE negative shifts (Fig. 2). The lower $\delta^{13}C$ shift (NL1) is believed to be

possibly correlated with the N1 counterpart of the Wa'ergang section of S. China,

which is immediately above the lower boundary of the conodont *Proconodontus*

posterocostatus Zone and that of Stage 10 too, and the upper shift (NL2) with N2 of

the Wa'ergang section were correlated with the overlying *Proconodontus muelleri*

Zone (Li et al., 2017). The Martin Point TOC and $\delta^{13}C_{org}$ profiles show lower values

correlated with NL1 and NL2, whereas the $\delta^{15}N_{org}$ exhibit a relative enrichment

correlated particularly with NL2 (Fig. 5).

The concentrations of the investigated elemental paleoenvironmental proxies (e.g., Tribovillard et al., 2006; Śliwiński et al., 2010; Acharya et al., 2015; Yao et al., 2017, Shembilu and Azmy, 2021) are tabulated in Appendix 1 and their statistics are summarized in Table 1. Their mean values are almost comparable to those documented for the overlying HERB carbonates although those of Ni, Cu, Zn, Fe, Al/Ti, and Th/U are generally lower (Table 1; Wang and Azmy, 2020). On the contrary, the mean-value counterparts documented for the older carbonate section spanning the base of the SPICE (Steptoean Positive Carbon Isotope Excursion) and top of DICE (Drumian Carbon Isotope Excursion) from Belle Isle (western Newfoundland) are considerably higher (Shembilu and Azmy, 2022 their Table 1).

The Sr values (308 ± 224 ppm; Table 1; Appendix 1) exhibit insignificant correlations with their P ($R^2 = 0.02$), Ni ($R^2 = 0.02$), Cu ($R^2 = 0.12$), Zn ($R^2 = 0.04$), Al ($R^2 = 0.004$), $\sum$REE ($R^2 = 0.05$), Mn ($R^2 = 0.09$), Fe ($R^2 = 0.06$), Th/U ($R^2 = 0.000001$), and δ^{18}O ($R^2 = 0.04$) values (Fig. 6a–j).

The enrichment factor profiles of the investigated elemental proxies display some variations correlated with the lower NL1 δ^{13}C shift but most of them (P, Ni, Cu, Zn, Al, $\sum$REE, Mn, and Fe) show a distinct minor positive shift at a level correlated with the lower part of the upper NL2 shift (Fig. 5). The $\sum$REE, Mn, and Fe profile show a general long-term trend of decrease upward (Fig. 5).

CHAPTER V

DISCUSSION

I – VI: Redox conditions across the Upper Cambrian of eastern Laurentia: implications from geochemical proxies (currently pending review in the Journal of Paleogeography, Paleoclimatology, Paleoecology).

5.1 Sample Preservation and Diagenetic Influence

5.1.1 Petrographic preservation

The petrographic preservation of the investigated samples has been discussed in detail by Azmy (2019b) and is therefore only summarized below. The petrographic examination shows that the samples are dominated by lime mudstones with insignificant recrystallization and preservation of almost pristine sedimentary fabrics (Fig. 3a). The grain size varies from micritic (<4 μm) to near-micritic (≤10 μm) and they appear dull to non-luminescent under cathodoluminoscope (CL) (Fig. 3b), thus suggesting low water/rock interaction ratios (e.g., Azmy, 2019a; Wang and Azmy, 2020).

The geochemistry of carbonates is known to control their luminescence, which is activated by the enrichment of Mn but quenched by high concentrations of Fe (Machel and Burton, 1991). Although, in many cases, dull CL reflects relative preservation of primary to near-primary geochemical signatures (e.g., Veizer et al., 1999), many late-burial cements may appear dull to non-CL owing to their high Fe contents (Rush and Chafetz, 1990). Nevertheless, the studied carbonates are lime mudstones of slope setting rhythmites (James and Stevens, 1986) of suboxic

conditions, where Fe and/or Mn are expected to be relatively enriched (Morrison and Brand, 1986; Azmy, 2019a). Therefore, cathodoluminescence is a preliminary petrographic evaluation tool that should be combined with additional screening tests to confirm sample preservation (Brand et al., 2011).

5.1.2 Preservation of geochemical signatures

Temperature increases with depth during the progressive burial of sediments through the diagenetic history, which results in thermal degradation of organic matter and loss of TOC. This may also lead to the release of compounds enriched in light ^{12}C and ^{14}N, which may increase the $\delta^{13}C_{org}$ and $\delta^{15}N_{org}$ values of remaining organic matter (Faure and Mensing, 2005). No exact range of burial temperatures has been documented specifically for the Martin Point carbonates by earlier studies, but the TOC contents exhibit a weak correlation with their $\delta^{13}C_{org}$ values ($R^2 = 0.2$; Fig. 4a), which argues for at least near-primary $\delta^{13}C_{org}$ values. On the other hand, the TOC values show a moderate correlation with their $\delta^{15}N_{org}$ counterparts ($R^2 = 0.4$; Fig. 4b) that might reflect some diagenetic impact although this is not supported by the insignificant influence of diagenesis on the associated $\delta^{13}C_{org}$ values, which suggests that other factors (e.g., environmental) might have some contributions to the moderate correlation.

During the burial history of carbonates, diagenetic alteration results in the enrichment of some elements such as Mn, Fe, Al, and $\sum$REE but depletion of others such as Sr (Veizer, 1983; Azmy et al., 2011; Wang and Azmy, 2020) in the diagenetic carbonates. Diagenesis has also an effect on the content of some paleoenvironmental proxies such as Ni, P, Zn, Cu, Th, and U but very little to insignificant, particularly at

low water/rock interaction ratios (e.g., Veizer, 1983; Śliwiński et al., 2010; Pattan et al., 2013; Acharya et al., 2015; Shembilu and Azmy; 2022).
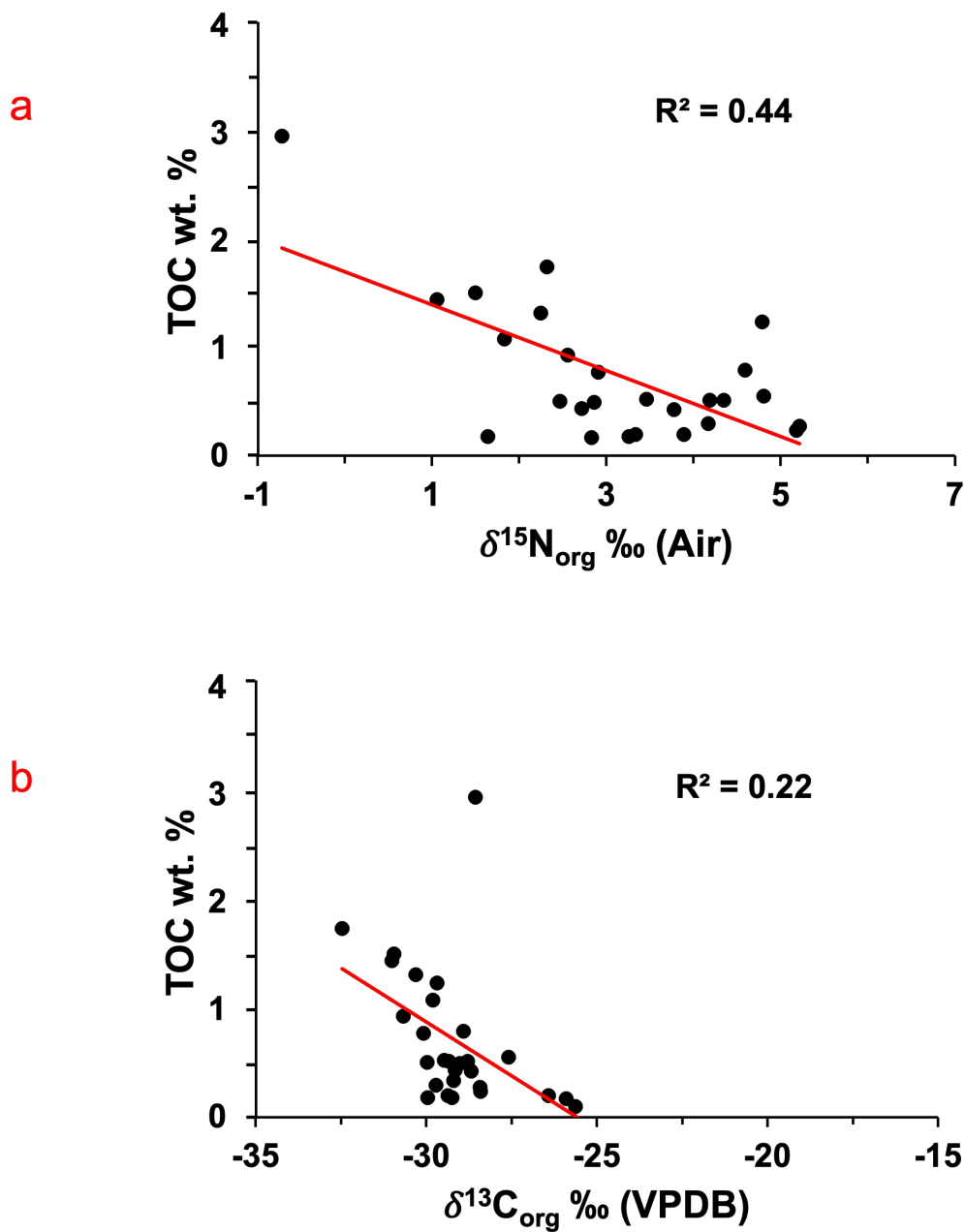
Fig. 4. Scatter plots showing correlations of (a) $\delta^{13}C$ and (b) $\delta^{15}N_{org}$ with TOC for the Martin Point lime mudstones.

The Sr concentrations of the investigated carbonates exhibit insignificant correlations (R^2 = <0.01–0.12) with the Mn, Fe, Al, REE, $\delta^{18}O$, and the other paleoenvironmental proxies (Fig. 6a–j). The lack of alteration trends is consistent with the petrographic preservation and argues for the preservation of at least near-primary signatures of those proxies. The Sr profile shows no negative shifts of diagenetic origin that can be correlated with counterparts on the profiles of other proxies (Fig. 5). Preservation of similar proxies has been documented for the younger uppermost Cambrian Martin Point carbonates (Wang and Azmy, 2020) and the older Middle-Upper Belle Isle carbonates (Shembilu and Azmy, 2022) of western Newfoundland.

Earlier studies suggested that the Cambrian was dominated by sealevel rise that caused ocean stratification and pumped organic matter, through shoaling, to the shallow environment, which likely caused possible dysoxic conditions (e.g., Li et al., 2018). This may explain the enriched Mn and Fe contents (291 ± 154 ppm and 1685 ± 1741 ppm, respectively; Table 1; Appendix 1) in the Martin Point carbonates, which is also consistent with the poor correlation of both element contents with that of Sr (Fig. 6g–h).

5.2 Redox and paleoenvironmental conditions

The $\delta^{13}C_{carb}$ profile of the outcropped Martin Point section exhibits two negative excursions above the SPICE event (lower NL1 and upper NL2; Figs. 2a and 5). The lower (NL1, 3 to 4 ‰) has been globally correlated with the lower *Proconodontus posterocostatus* Zone (base of the Stage 10) and the upper (NL2, 5 to 6 ‰) with the *P. muelleri* Zone (Li et al., 2017; Azmy 2019b; Zhao et al., 2022).
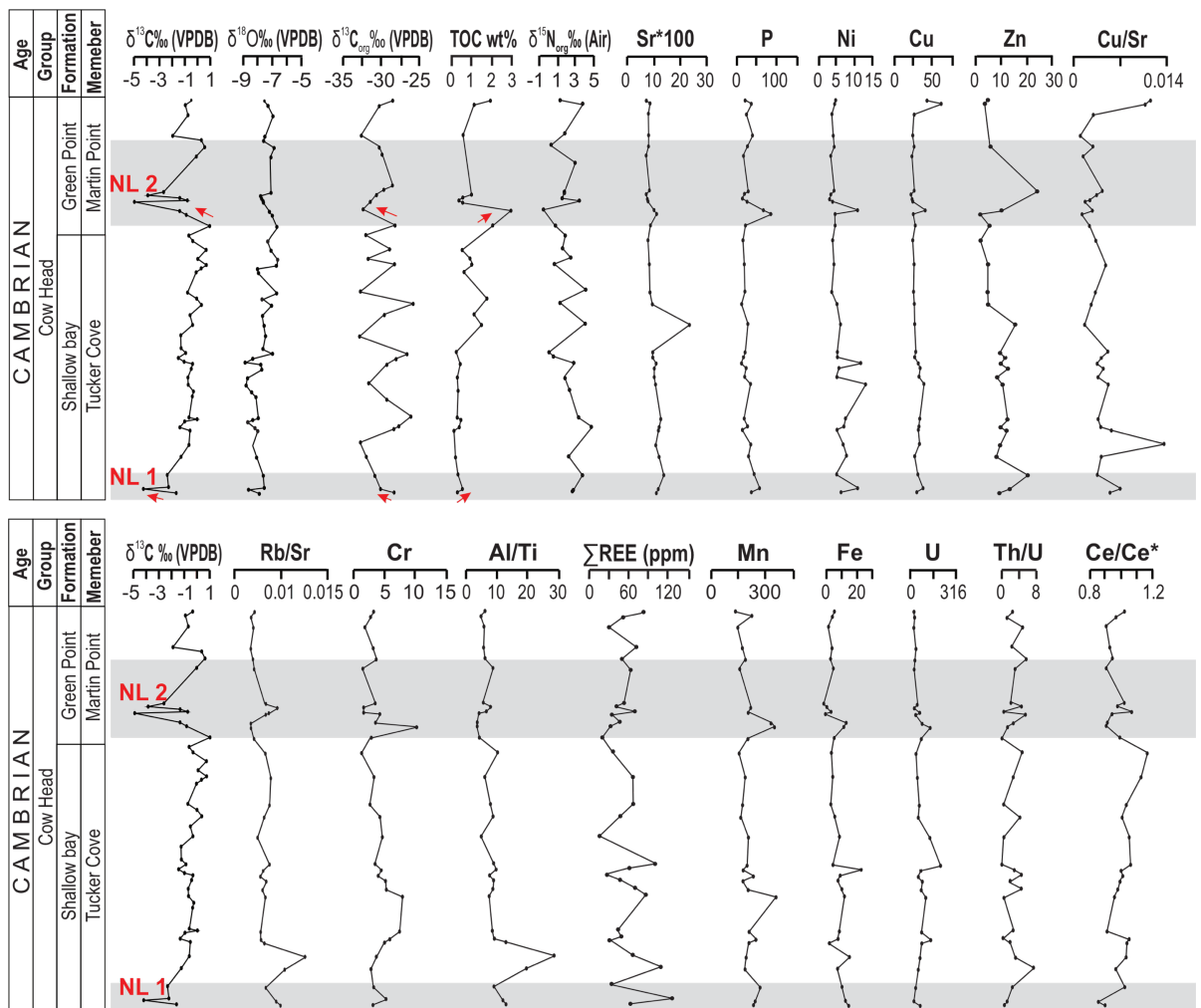
Fig. 5. Paleo-environmental proxy profiles (constructed from enrichment factor values) of Martin Point carbonates across the investigated interval. The $\delta^{13}C_{carb}$ and $\delta^{18}O$ profiles are derived from Azmy (2019b). The NL1 and NL2 intervals are highlighted in grey. Arrows show the correlated variations on the $\delta^{13}C_{carb}$, $\delta^{13}C_{org}$, and TOC profiles.

However, the *muelleri* and the underlying *posterocostatus* zones, or possibly their equivalents, have not yet been documented in the section, and the chemostratigraphic correlation must be taken with caution. These two shifts occur directly below the HERB negative $\delta^{13}C_{carb}$ excursion and have been correlated with counterparts (N1 and N2, Fig. 2b) in the Wa'ergang section of S. China (Li et al., 2017; Azmy 2019b, his figure 2).

Eustatic sealevel variations have occurred repeatedly and cyclically throughout the geologic time and had a significant impact on ocean primary productivity, redox condition, and inputs of terrigenous materials from weathering, which in turn affected the physical and geochemical characteristics (isotopic and trace elements concentrations) of marine carbonates (Pitman, 1978; Brasier, 1982; Cowan and James 1993; Wignall and Twitchett, 1996; Algeo and Sheckler 1998; Arnaboldi and Meyers, 2007; Algeo and Maynard, 2008; Śliwiński et al., 2010; Archaya et al., 2015; Pagès and Schmid, 2016; Zhang et al., 2022).

Generally speaking, the depletion in ^{13}C of marine carbonate C-isotope compositions has been found to be influenced by diagenesis, eustatic sealevel changes, organic bioproductivity, and evolution of seawater through the Earth's history (e.g., Veizer, 1983; Veizer et al., 1999; Immenhauser et al., 2008; Oehlert and Swart, 2014; Swart, 2015). The evaluation of the degree of preservation of the $\delta^{13}C_{carb}$ values of the investigated lime mudstones (micritic - no dolomites) has been discussed in detail by Azmy (2019b). Their insignificant correlations with diagenetic proxies (e.g., Sr, Al, Mn, Fe, and $\delta^{18}O$) suggest minimum alteration and preservation of at least near-primary signatures. The evolution of the $\delta^{13}C_{carb}$ of the seawater during the

Late Cambrian (e.g., Veizer et al., 1999; Schmid, 2017) does not show a long-term dramatic change (~ 1 ‰) and no evidence of significant glaciations during that time interval has been documented either.

Recent studies of the $\delta^{13}C_{carb}$ of Middle–Upper Cambrian carbonates (e.g., Miller et al., 2011; Li et al., 2020), particularly those of the Wa'ergang section in S. China (Li et al., 2017; equivalent to the investigated Martin Point interval), documented distinct negative $\delta^{13}C_{carb}$ excursions that were suggested to have been caused by two different scenarios. It is possible that negative $\delta^{13}C_{carb}$ excursions reflect the influence of sealevel drop that brought oxygenated surface water in contact with buried organic matter, which released light $^{12}CO_2$ and the effect was enhanced by the input of organic matter associated with terrigenous inputs due to the increase in the land areas exposed to weathering (e.g., Li et al., 2017). Alternatively, sea transgression was associated with shoaling of organic-rich anoxic water into oxic shallow settings where oxygen was highly consumed by oxidation of organic matter to release light $^{12}CO_2$ and led to dysoxic conditions in shallow marine environments (e.g., Pagés and Schmid, 2016; Pagés et al., 2016; Schmid, 2017; Li et al., 2020). The response of elemental proxies is expected to be different in both scenarios and the associated variations in elemental geochemistry (environmental paleoproxies) may therefore reveal the nature of sealevel changes and variations in seawater water chemistry because they reflect the impact of inputs of terrestrial material and nutrients and redox conditions on primary productivity (e.g., Kimura et al., 2005; Arnaboldi and Meyers, 2007; Wignall et al., 2007; Śliwiński et al., 2010; Pattan et al., 2013; Acharya et al., 2015; Pagés and Schmid, 2016; Liyuan et al., 2021; Zhang et al., 2022).
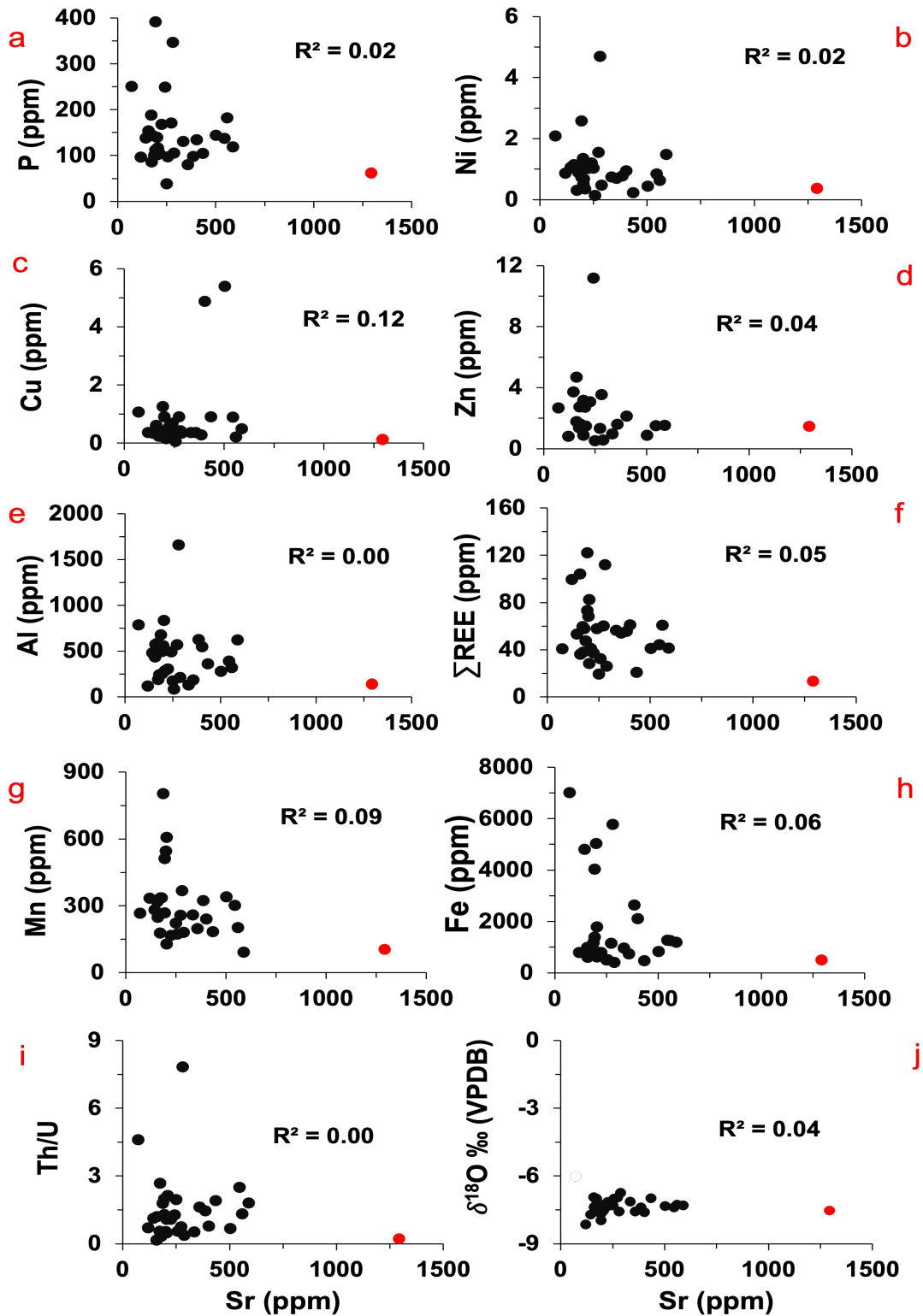
Fig. 6. Scatter plots showing correlations of Sr with (a) P (b) Ni (c) Cu (d) Zn (e) Al (f) ∑REE (g) Mn (h) Fe (i) Th/U and (j) δ^{18}O for the investigated Martin Point section. The R^2 values are calculated without Sample B23-9 that has the odd high Sr contents (Appendix 1).

Primary negative $\delta^{13}C_{carb}$ excursions caused by sealevel drop are expected to be associated with the exposure of more land area, which will increase the riverine and/or wind-blown inputs of weathered terrestrial material and will also be reflected by a relative increase in the weathering paleoenvironmental proxies (Al, REE, and possibly Mn and Fe) and nutrient proxies (P, Ni, Cu) contents (e.g., Tribovillard et al., 2006; Śliwiński et al., 2010). If the consumption of oxygen in the surface water by the organic matter buried at relatively deeper settings was not too extensive (i.e., general suboxic conditions), the paleoredox proxies, such as the Th/U and Ce/Ce* (Wignall and Twitchett, 1996; Kimura et al., 2005; Arnaboldi and Meyers, 2007; Wignall et al., 2007), may still show some associated variations reflecting a relative increase in oxic conditions (e.g., Wang and Azmy, 2020; Shembilu and Azmy, 2022) and possible pulses of enhancement in primary productivity despite the dominating general dysoxic conditions. The $\delta^{13}C_{org}$ and TOC profiles may therefore exhibit some correlated increase (Wang and Azmy, 2020).

However, this is not the case for the NL1 and NL2 of the Martin Point section (Fig. 5). The investigated carbonates are rhythmites of slope deposits (James and Stevens, 1986) where lime mudstones are interbedded with shales and siltstones. Therefore, it is more reliable to normalize the elemental compositions to Al and use the variations of the enrichment factor in order to eliminate the influence of siliciclastic inclusions on the signatures of elemental paleoproxies. (Fig. 5; Kryc et al, 2003; Tribovillard et al., 2006). Crustal rocks are mainly enriched in Al and Ti, which are widely used for normalizing trace elements in carbonates to eliminate their contributions from terrestrial inputs (Tribovillard et al., 2006). In marine carbonates with low detrital fraction, Al is scavenged as hydroxides coating biogenic particles

(Kryc et al, 2003; Zhang et al., 2022) and an attempt for correction may obscure the actual elemental signature. Therefore, Ti was introduced for normalization although it can be removed by organic matter (Kryc et al., 2003). However, the Martin Point carbonates are not biogenic-rich, which argues for the validity of using Al for normalization and the reliability of the calculated enrichment factors.

5.2.1 NL2 Geochemical variations:

The base of the NL2 negative $\delta^{13}C_{carb}$ is correlated with a positive shift/pulse on the profiles of TOC, P, Ni, Cu, Cr, $\sum$REE, Mn, Fe, and U where these pulses are followed by a drop/negative shift shown by most of the profiles (Fig. 5). Deeper anoxic water is expected to be enriched in organic matter and micronutrient (e.g., P, Ni, Cu, and Zn) among other elements that are usually adsorbed on organic matter or enriched in low-oxygen conditions (e.g., Cr, $\sum$REE, Mn, Fe, and U). Therefore, a transgression at the base of the NL2 excursion might have been associated with a pulse of shoaling of organic-rich anoxic waters into an oxygenated shallow environment. Oxidation of organic matter released light $^{12}CO_2$ that led to a negative shift in the $\delta^{13}C_{carb}$ and a decrease in TOC contents as well as an increase in the $\delta^{13}C_{org}$ (Fig. 5) due to preferential removal of light ^{12}C through oxidation, which is consistent with a drop in TOC contents and enrichment in the $\delta^{13}C_{org}$ correlated with NL2. This also agrees with a correlated positive shift on the Zn profile that reflects a decrease in primary productivity since zinc is a trace micronutrient and known to be also consumed by organic productivity (e.g., Conway and John, 2014; Kunzmann et al., 2013). The oxidation of Zn-rich organic matter released also more Zn that enhanced the effect. In addition, the $\delta^{15}N_{org}$ profile shows a negative pulse at the base

of NL2 that inflects into a positive shift throughout NL2 (Fig. 5), which is consistent

with the initial emplacement of organic matter (enriched in ^{14}N) during shoaling that

resulted in dysoxic conditions, by consuming oxygen, and enrichment in the $\delta^{15}N_{org}$

values due to the effect of nitrate-reducing bacterial in a low-oxygen environment.

This agrees with the Ce/Ce* profile that shows correlated values close to unity (0.8–

0.9) during the NL2 event (Fig. 5).

Although $\delta^{18}O_{carb}$ is extremely sensitive to diagenetic alteration (Veizer,

1983), the poor correlation of Sr with $\delta^{18}O_{carb}$ ($R^2 = 0.04$; Fig. 6j; Azmy, 2019b)

suggests that the investigated carbonates might retain some near-primary $\delta^{18}O_{carb}$

signatures (e.g., Schiffbauer et al., 2017) and their variations has to be therefore taken

with caution. The $\delta^{18}O_{carb}$ profile shows a wide slight negative excursion (~ 1.5‰)

correlated with NL2 (Fig. 5) that implies relatively warmer conditions consistent with

a transgressive event.

Using elemental ratios as paleoproxies is, at times, more reliable than absolute

concentrations because it eliminates the influence of lithology. Therefore, Cu/Sr,

Rb/Sr, and Al/Ti may be used as climate proxies (e.g., Zhang et al., 2022). The

concentration of sedimentary Sr increases by evaporation of seawater and the

precipitation of $SrSO_4$ during warm conditions (e.g., Lerman, 1978). Therefore, lower

Sr contents may suggest a humid climate, whereas higher contents may reflect an arid

climate. By contrast, Rb and Cu are immobile in sediments, which makes the low

Cu/Sr and low Rb/Sr ratios proxies of arid conditions and vice versa (Lerman et al.,

1995, Zhang et al 2022) although the Sr is significantly more enriched in aragonite

than in calcite and the interpretation of these ratios have to be taken with caution.

However, the Sr values of the Martin Point carbonates (Fig. 6), except for one sample, are generally Low (276 ± 136 ppm) and their profile (Fig. 5) does not exhibit enrichments correlated with the NL2 or NL1 events.

In addition, taking into consideration the abundance of Al relative to Ti in crustal rocks (Taylor and McLennan, 1985; McLennan, 2001) and the general minor variations exhibited by the Al/Ti profile (Fig. 5), the influence of scavenging of Al by hydroxides or Ti by organometallic compounds is expected to be insignificant in the investigated organic-poor Martin Point carbonates (Kryc et al., 2003).

The Cu/Sr and Rb/Sr profiles (Fig. 5) exhibit insignificant variations correlated with NL2 that might have been caused by minor fluctuations in terrigenous inputs (riverine during humid climates), which is also consistent with the correlated insignificant shift on the Al/Ti profile (cf. Kryc, et al., 2003). This agrees with the profiles of the micronutrient (P, Ni, and Cu), TOC, elements enriched in crustal rocks ($\sum$REE, Mn, and Fe) that do not exhibit correlated considerable enrichments with NL2 (Fig. 5), and they were therefore likely sourced from the shoaling anoxic waters.

In oxidizing environments, U ions occur in the water column as $[U^{6+}]$ that form the soluble uranyl carbonate whereas, in reducing conditions, they retain the lower oxidation state $[U^{4+}]$ and form the insoluble uranous fluoride, which is trapped in marine carbonates (Wignall and Twitchett, 1996). On the other hand, Th is not affected by redox conditions and occurs permanently in the insoluble $[Th^{4+}]$, which makes the sediments of anoxic environments lower in Th/U ratio than those of oxic environments. Ce anomaly in marine carbonates (a paleo-seawater redox proxy) usually depicts a negative shift (~ 0.4 – 0.5) for oxic waters (German and Elderfield,

1990; Bau and Dulski,1996), and this is due to the oxidation of Ce^{3+} in aqueous systems to Ce^{4+} on the surfaces of suspended particles (Bau and Dulski, 1996), thereby leaving shallow oxic water depleted in Ce. The Martin Point Th/U profile (Fig. 5) shows minor fluctuations correlated with the NL2 event whereas the Ce/Ce* values are generally around the unity (1.1 ± 0.1) throughout the entire profile, which supports dysoxic conditions (Table 1; Fig. 5).

Thus, the geochemical evidence from micronutrients (P, Ni, Cu, and Zn), paleoenvironmental (Cr, $\sum$REE, Mn, Fe, U, Cu/Sr, Rb/Sr, Al/Ti, and $\delta^{18}O_{carb}$) and paleoredox proxies, and $\delta^{13}C_{org}$, $\delta^{15}N_{org}$, and TOC values of the organic matter suggests that the post-SPICE NL2 event was likely caused by a sea transgression, during warm and possibly humid climate, that brought anoxic water enriched in organic matter to the shallow water environment and resulted in dysoxic conditions (e.g., Li et al., 2020). This also agrees with the conclusions of earlier sedimentological studies of the Martin point slope carbonates (Landing et al., 2002; Landing, 2012, 2013; Landing and Webster, 2018).

5.2.2 NL1 Geochemical variations:

Although the $\delta^{13}C_{carb}$ profile shows that NL1 has a distinct negative shift, many of the proxy profiles might not show detailed or highly resolved correlations like those of NL2 (Fig. 5) since no more beds at the lower stratigraphic levels were outcropped or accessible for sampling in the Martin Point section. Thus, the negative $\delta^{13}C_{carb}$ of NL1 likely constitutes the upper part of that negative excursion, which makes the interpretations based on a few points and to be taken with caution.

Similar to NL2, NL1 is correlated with low TOC and a general depletion in $\delta^{13}C_{org,}$ but a slight increase in $\delta^{15}N_{org}$ (Fig. 5), which support a similar scenario of transgression and shoaling of anoxic organic-rich waters. The $\delta^{18}O_{carb}$ profile (Fig. 5) also shows a correlated slight negative shift (~ 1‰) similar to that of NL2 and consistent with warmer weather during NL1.

The profiles of micronutrients (P, Ni, Cu, and Zn) and ∑REE exhibit correlated but smaller enrichment pulses compared with those associated with NL2 and the trend of Zn reflects similar low organic productivity. However, the Mn profile shows a general slight increase and that of Fe a decrease. These variations also favor a transgression scenario similar to that of NL2. However, the Cu/Sr profile shows a general slight decrease similar to that of the Rb/Sr and Al/Ti counterparts, which may reflect insignificant contributions from the terrigenous inputs. Thus, a transgression scenario similar to that of NL2 likely caused the NL1 event.

5.2.3 The interval between NL1 and NL2:

Unlike the NL1 and NL2 negative $\delta^{13}C_{carb}$ shifts, the interval between them shows a wide positive $\delta^{13}C_{carb}$ excursion (~ 6‰) that correlates with fluctuated enrichments in the TOC and a similar pattern of the $\delta^{13}C_{org}$ that may reach up to – 25 ‰ (Fig. 5). This may suggest that this time interval had at least higher organic productivity and relatively less dysoxic condition than the times of the NL1 and NL2 events, which is consistent with the $\delta^{15}N_{org}$ profile that shows a correlated slight upward long-term depletion (due to relative lower activity of nitrate-reducing bacteria) across the positive $\delta^{13}C_{carb}$ excursion (Fig. 5). Micronutrients, such as the Ni profile, show some enrichment only at a level correlated with the lower part of the

excursion and the Zn counterpart shows no distinct increase like that correlated with NL1 and NL2, which supports the suggested relative increase in primary productivity although P and Cu exhibit almost no variations (Fig. 5). The Al/Ti, $\sum$REE, Mn, and Fe profiles show some fluctuating enrichment correlated with the lower part of the excursion reflecting possible relative enhancement in terrigenous inputs. However, the correlated enrichment in Cr (Fig. 5) argues against dramatic riverine inputs by a significant eustatic sealevel drop of global icehouse mode but likely for dysoxic conditions. This is supported by the general slight enrichment of U, minor negative excursion of the Th/U, and the positive excursion of the Ce/Ce* (Fig. 5) that do not support dramatic oxic conditions as expected from enhanced circulations during a major sealevel drop.

Thus, the enhancement in organic productivity, particularly at the lower part of the positive excursion, was caused by contributions from terrigenous material possibly due to some increase in riverine inputs during sealevel fluctuations or relative sealevel drop under a dominant greenhouse period (e.g., Wang et al., 2021; Xia et al., 2023). Terrigenous materials often display a REE distribution pattern generated by the mixing of saltwater and freshwater, which will likely impact the seawater composition of modern platform facies (e.g., Johannesson et al., 2006). Modern carbonates of oxic tropical shallow-water settings have Y/Ho values of 47 to 70 (cf. Li et al., 2019; Liu et al., 2022, Xia et al.,2023) and siliciclastic inclusions have been found to lower this ratio in carbonates (cf. Liu et al., 2022). However, the Martin point carbonates have generally low Al contents (438 $\pm$ 301; Table 1) and their Y/Ho values, particularly within the positive $\delta^{13}C_{carb}$ excursion interval (Y/Ho = 30 $\pm$ 3; Appendix 1), are considerably lower than their modern counterparts (57 $\pm$ 17; Li et al., 2019), which

dismisses any scenario of major sealevel drop associated with upwelling and dramatic oxygenation of icehouse mode. This is supported by the lack of globally documented glacial deposits during this time interval. Enhancement in continental chemical weathering would consume light atmospheric $^{12}CO_2$ and lead to a cooler climate and relatively more ^{13}C-enriched marine carbonates (Fig. 5; Appendix 1).

The general narrow range of variations in the $\delta^{18}O$ values throughout its entire profile, and particularly within the wide interval between NL1 and NL2 (Fig. 5), makes it difficult to see a sharp trend. However, the values show a general slightly increasing trend ($\sim$ 1‰) through the lower part of the wide positive $\delta^{13}C$ excursion that decreases in the upper part of the excursion, thus reflecting a possible minor increase in warming conditions towards the end of the positive $\delta^{13}C$ excursion. This is consistent with the correlated fluctuating enrichments shown by the Al/Ti, $\sum$REE, and Mn profiles, and the suggested sealevel fluctuation (possible relative drop during the lower part of the excursion) and slight increase in terrigenous inputs. However, this has to be taken with caution since the variations in the $\delta^{18}O$ values are not big and the influence of diagenesis cannot be entirely dismissed because the $\delta^{18}O$ is highly sensitive to diagenetic alteration (Veizer, 1983).

Although this positive $\delta^{13}C$ excursion does not correlate with a global stratigraphic boundary and may not contribute significantly to global chemostratigraphic correlations, it has, to some extent, similarities with those of the SPICE event such as the comparable $\delta^{13}C$ amplitude/strength and bracketing by negative $\delta^{13}C$ excursions. Therefore, the correlated paleoproxy variations may shed light on the paleoenvironmental conditions that dominated during the SPICE event

and allow a better understanding of the mechanism that led to those settings (e.g., Saltzman et al., 2004; Gill et al., 2011).

The Sr profile (enrichment factor) shows a distinct peak of enrichment (1294 ppm; Fig. 5; Appendix 1) at a stratigraphic level correlated almost with the middle of the positive $\delta^{13}C_{carb}$ excursion (Fig. 5). This is opposite to the expected depletion of Sr in diagenetic calcite, which may imply that it is a reflection of another controlling factor such as a precursor aragonitic lime mudstone caused by possible alternations between aragonitic and calcitic seas. Comparable high Sr contents have been recorded in the Upper Cambrian Martin Point carbonates (e.g., Wang and Azmy, 2020) and earlier studies also documented the occurrence of aragonite cements in the Late Cambrian shallow-warm tropical environment (Neilson et al., 2016). However, interpreting such sudden enrichments in Sr is suggested to be taken with caution until more targeted studies reveal their nature.

5.3 Post-SPICE (NL1 & NL2) vs HERB

The Martin Point section consists of rhythmites (alternating lime mudstone and shale interbeds) where the post-SPICE interval spans the lower part of the section, and the HERB event covers most of the upper part. The preservation of the petrographic textures (micritic to near-micritic fabric) and geochemical signatures of the HERB carbonates have been evaluated and discussed by Wang and Azmy (2020). Similar to the post-SPICE carbonates of NL1 and NL2 events, the $\delta^{13}C_{org}$ and $\delta^{15}N_{org}$ values of the HERB carbonates exhibit insignificant correlations with their TOC counterparts ($R^2 = 0.02$ and 0.0003 respectively). The correlation of Sr with P, Ni, Cu, Zn, Al, $\sum$REE, Mn, Fe, Th/U and $\delta^{18}O$ showed poor correlations <0.32. The HERB

enrichment factor profiles of the paleoenvironmental proxies were reconstructed from the trace element results of Wang and Azmy (2020). The $\delta^{13}C_{carb}$ profile shows a negative excursion with a peak that marks the base of the conodont *Econodontus notchpeakensis* Zone (Fig. 7).
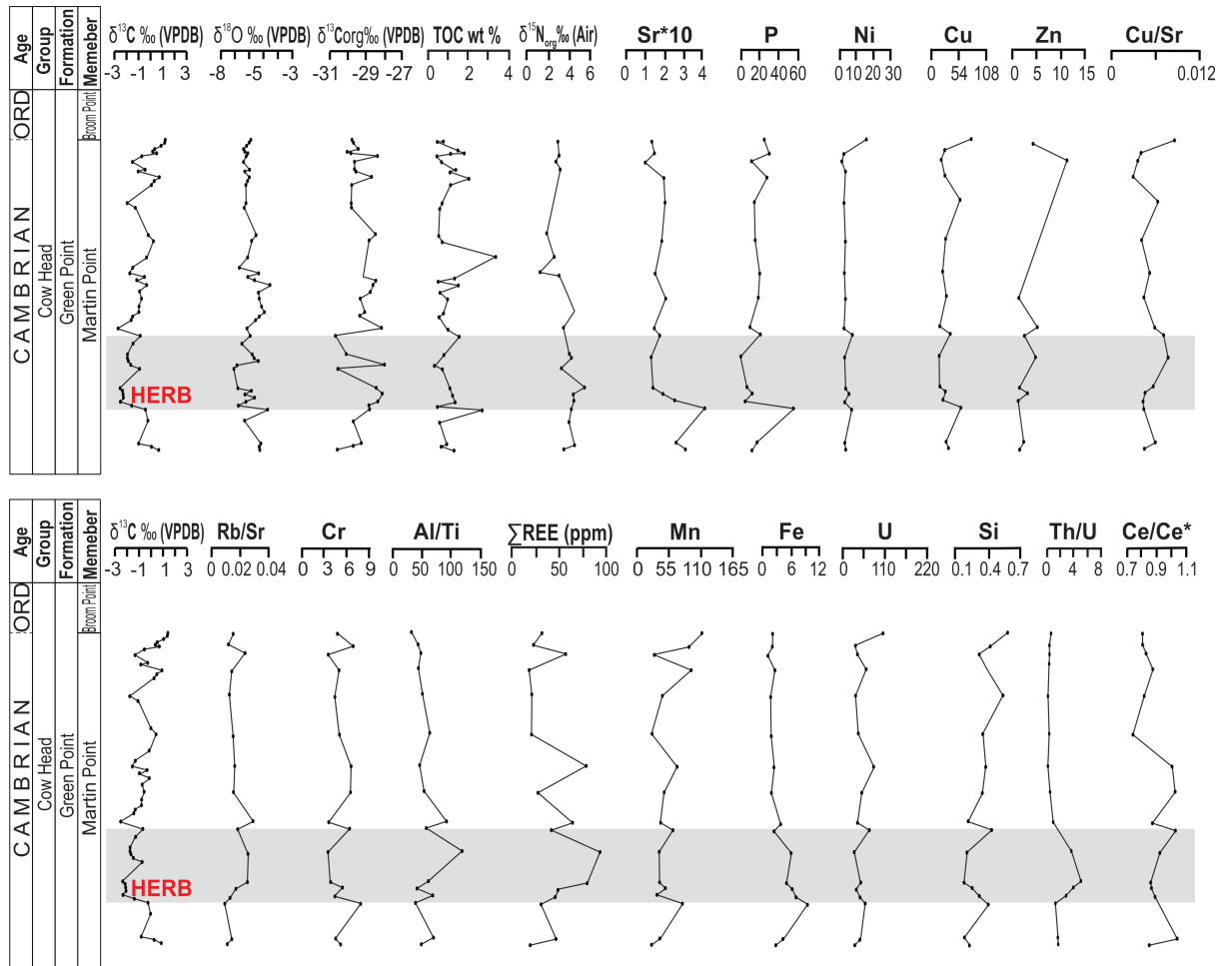
Fig. 7. Paleo-environmental proxy profiles (constructed from enrichment factor values) of Martin Point carbonates across the investigated HERB interval (data from Wang and Azmy, 2020). The HERB interval is highlighted in grey.

The mean $\delta^{13}C_{carb}$ values of the post-SPICE and the overlying HERB carbonates

(Table 1; Appendix 1) are nearly comparable (cf. Wang and Azmy, 2020) and

similarly those of $\delta^{18}O$, $\delta^{13}C_{org}$, TOC, $\delta^{15}N_{org}$, Sr, P, $\sum$REE, U, Th/U, and Ce/Ce*.

However, those of Ni, Cu, Cr, Zn, and Rb/Sr are higher in the HERB carbonates

(Table 1; Fig. 8).

The peak of the HERB negative $\delta^{13}C_{carb}$ excursion correlates with a broad

positive $\delta^{13}C_{org}$ excursion although the TOC profile shows a slight increase followed

by a decrease immediately after a distinct enrichment of ~2.5 % at the base of the

HERB event (Fig. 7). The TOC profile also shows a wide positive shift at the top

(~3.0 %) of the Martin Point section (Fig. 7). Like the post-SPICE profiles, the HERB

TOC, P, Ni, Cu, Cr, $\sum$REE, Mn, Fe, and U profiles show minor pulses of enrichment

near the base of the HERB event, followed by a drop/negative shift (Fig. 7) like their

post-SPICE counterparts. Thus, the variations in the TOC profile and the correlated

negative $\delta^{13}C_{org}$ suggest that the HERB event started with a transgression (Miller et

al., 2011), similar to that of the post-SPICE NL1 and NL2 events, which was

associated with shoaling of deeper anoxic water enriched in organic matter. The

elements adsorbed on the organic matter (e.g., P, Ni, Cu, Cr, $\sum$REE, Mn, Fe, and U)

were likely the reason behind the pulse of initial enrichment that was inflected into a

depletion after the oxidation of the organic matter in the shallow water. The oxidation

of organic matter released light $^{12}CO_2$ and consumed oxygen, thus resulting in dysoxic

conditions (Wang and Azmy, 2020). This is supported by the correlated relative

enrichment in the $\delta^{15}N_{org}$, lower Al/Ti, and Si (lower weathering rates during

transgression) that support insignificant contributions from terrigenous inputs at the base and peak of the HERB negative $\delta^{13}C_{carb}$ excursion (Fig. 7).
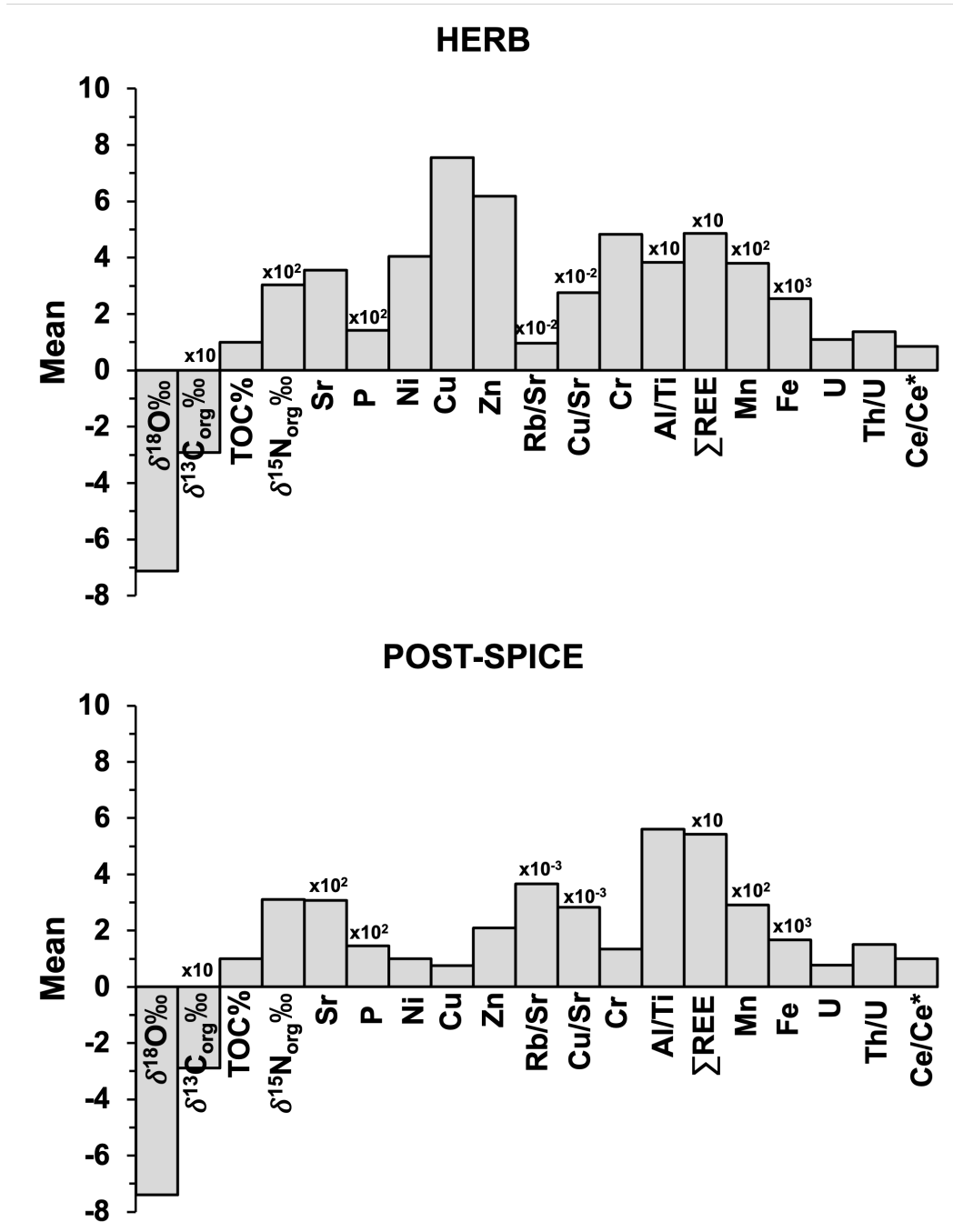
Fig. 8. Histograms depicting the mean concentrations of the paleo-environmental proxies used for (a) SPICE and (b) HERB Events in the investigated Martin Point section.

However, after the peak of the excursion, the TOC profile shows a gradual enrichment correlated with a wide negative $\delta^{13}C_{org}$ shift and positive Al/Ti shift (Fig. 7). This may suggest that the shoaling of organic matter during the main course of sealevel rise and transgression was followed by a possible interrupting sealevel drop that might have resulted in a relatively minor increase in primary productivity under the dysoxic conditions due to slight enhancement of inputs from weathered crustal material. This is supported by the relative depletion in $\delta^{15}N_{org}$ although the P, Ni, Cu, Zn (micronutrients), Rb/Sr, and Cu/Sr profiles do not show significantly correlated swings (Fig. 7).

The Ce/Ce* values are close to unity, which supports the dominant dysoxic conditions (Wang and Azmy, 2020) and the transgression scenario (Fig. 7). In addition, Miller et al (2011) postulated that Red Top member of the Notch Peak Formation in western Utah, which archives the HERB event, was deposited in a low stand system tract during a relative sealevel rise evident by the deposition of thin layers of stromatolite biostrome at Lawson cove area, USA.

However, Th/U exhibit an unexpected consistent positive shift that correlates with the HERB event despite the dysoxic conditions suggested by other proxies and transgression scenario. The enrichment in Th/U ratio is known to reflect enhancement in oxic conditions (Wignall and Twitchett, 1996), which can be achieved by significant sealevel drop and well-mixed and well-oxygenated oceans during cold episodes of active upwelling. However, the Y/Ho values of the HERB lime mudstones (34 ± 7; Appendix 1) are similar to those of the carbonates in lower Martin Point section and significantly lower than those of oxic modern water counterparts (57 ± 17;

Liu et al., 2022). This argues against any significant sealevel drop and upwelling associated with icehouse well-mixed and oxygenated oceans.

Although the mean Th/U values of the HERB and post-SPICE Martin Point carbonates are comparable (1.4 ± 1.5 and 1.5 ± 1.5, respectively), the Th/U profile shows a consistent positive shift correlated with the negative $\delta^{13}C$ of the HERB event (Fig. 7). This may suggest a relative decrease in the dysoxic conditions towards the peak of the event. The HERB sediments are believed to have been deposited during sea transgression of low stand system tract (LST, Miller et al., 2011). Thus, the positive Th/U suggests a relative increase in oxygenation associated usually with sealevel drop, which would have a conflict with the suggested transgression and shoaling of organic matter.

A possible reconciliation scenario is that the LST usually starts with lower rate of sealevel rise (Coe, 2003) causing sediments to prograde rather than aggrade and the slope carbonate interbeds (transported by currents) might have preferentially recorded the high Th/U signatures of the oxic shallower water due to sealevel fluctuations, which is consistent with the correlated increase in $\sum REE$. A third possible scenario is a decrease in the seawater U budget associated with a basinal restriction by a local barrier (e.g., Li et al., 2022) or with the global expansion of dysoxic conditions that lead to the rise of Th/U for that time interval. Therefore, the Th/U redox proxy has to be taken with caution.

Although minor alteration may cause significant changes in the $\delta^{18}O$ signature of carbonates, the poor correlation of Sr with $\delta^{18}O$ may support the preservation of

some near-primary signatures. The long-term slight depletion exhibited by the HERB

$\delta^{18}O$ Profile (Fig. 7) implies continuous warm conditions during the Upper Cambrian.

CHAPTER VI

CONCLUSION

- The petrographic and geochemical examinations of the Upper Cambrian Martin Point carbonates (rhythmites) indicate that they retain at least near-primary signatures of paleoenvironmental proxies including those of weathering (Cu/Sr, Rb/Sr, $\sum$REE, Al/Ti, and Sr), bioproductivity ($\delta^{13}C_{org}$, $\delta^{15}N_{org}$, TOC, P, Ni, Cu, and Zn), and paleoredox (Cr, Ce/Ce*, Mn, Fe, U, Th/U).

- The globally documented post-SPICE negative $\delta^{13}C_{carb}$ excursions (NL1 and overlying NL2) recorded by the investigated section were found to correlate with basal positive pulses in the TOC, P, Ni, Cu, Cr, $\sum$REE, Mn, Fe, and U profiles that are followed by a drop. This may reflect a possible shoaling of organic-rich anoxic waters into an oxygenated shallow environment that released light $^{12}CO_2$ and led to a negative shift in the $\delta^{13}C_{carb}$ and a decrease in TOC contents as well as an increase in the $\delta^{13}C_{org}$ due to preferential removal of light ^{12}C through oxidation.

- However, the $\delta^{15}N_{org}$ profile shows a negative pulse at the base of NL2 that inflects into a positive shift throughout the event, which is consistent with the initial emplacement of organic matter (enriched in ^{14}N) that led to more dysoxic conditions and later enrichment in the $\delta^{15}N_{org}$ by nitrate-reducing bacterial. This agrees with the Ce-anomaly values around the unity (0.8–0.9).

- Despite the expected influence of diagenesis on the $\delta^{18}O_{carb}$ values, they still have a poor correlation with Sr ($R^2 = 0.04$) and exhibit a wide slight negative

excursion (~ 1.5‰) correlated with NL2, suggesting warm conditions consistent with a transgressive event.

- Since NL1 spans only a few lowermost-outcropped beds of the Martin Point section, it represents the topmost part of the event. Thus, variations in some of the proxy profiles are not at a high resolution like those of NL2. However, the variations of proxies that are still comparable may suggest a similar scenario to that of NL2.

- The interval between the NL1 and NL2 events shows a positive $\delta^{13}C_{carb}$ excursion (~ 6‰) that correlates with variations in paleoenvironmental proxies, which support higher primary productivity due to enhanced terrigenous inputs possibly by riverine inputs during sealevel fluctuations but no evidence to support a major sealevel drop by an icehouse effect.

- This positive excursion has, to some extent, a similarity with that of the earlier SPICE event and the associated variations in paleoproxies may shed light on or contribute to better understanding of the driving forces of the SPICE event.

- The similarities between the concentrations and behavior of most of proxies of post-SPICE (NL1 and NL2) and HERB carbonates from the Martin Point section suggest no substantial changes in the elemental chemistry of the seawater through the Late Cambrian.

- The scenario of shoaling organic-rich water into shallow environment seems to be the mechanism that also triggered the HERB event. However, a minor relative increase in the primary productivity, under the dominant dysoxic conditions, occurred after the peak of the event and was reflected by a small

enrichment in the TOC contents and a negative shift (~2 ‰) in the $\delta^{13}C_{org}$

profile.

REFERENCES

Abshire, M.L., Romaniello, S.J., Kuzminov, A.M., Cofrancesco, J., Severmann, S. Riedinger, N., 2020. Uranium isotopes as a proxy for primary depositional redox conditions in organic-rich marine systems. Earth and Planetary Science Letters, 529, 115878.

Acharya, S. S., Panigrahi, M. K., Gupta, A. K., Tripathy, S., 2015. Response of trace metal redox proxies in continental shelf environment: The Eastern Arabian Sea scenario. Continental Shelf Research, 106, 70-84.

Algeo, T.J., Scheckler, S.E., 1998. Terrestrial-marine teleconnections in the Devonian: links between the evolution of land plants, weathering processes, and marine anoxic events. Philosophical Transactions of the Royal Society of London. Series B: Biological Sciences, 353, 113-130.

Algeo, T. J., Maynard, J. B., 2004. Trace element behavior and redox facies in core shales of Upper Pennsylvanian kansas-type cyclothems. Chemical Geology, 206, 289-318.

Algeo, T.J., Maynard, J.B., 2008. Trace-metal covariation as a guide to water-mass conditions in ancient anoxic marine environments. Geosphere, 4, 872-887.

Allen, P. A., Burgess, P. M., Galewsky, J., Sinclair, H. D., 2001. Flexural-Eustatic numerical model for drowning of the Eocene perialpine carbonate ramp and implications for Alpine geodynamics. Geological Society of America Bulletin, 113, 1052-1066.

Ansari, A.H., Singh, V.K., Sharma, M. and Kumar, K., 2022. High authigenic Co

 enrichment in the non-euxinic buff-grey and black shale of the Chandarpur

 Group, Chhattisgarh Supergroup: Implication for the late Mesoproterozoic

 shallow marine redox condition. Terra Nova, 34, 72-82.

Arnaboldi, M., Meyers, P. A., 2007. Trace element indicators of increased primary

 production and decreased water column ventilation during deposition of Latest

 Pliocene sapropels at five locations across the Mediterranean Sea.

 Palaeogeography, Palaeoclimatology, Palaeoecology, 249, 425-443.

Azmy, K., 2019a. Carbon-isotope stratigraphy of the Uppermost Cambrian in eastern

 Laurentia: Implications for global correlation. Geology Magazine, 156, 759-

 771.

Azmy, K., 2019b. Carbon-isotope stratigraghphy of the SPICE event (Upper

 Cambrian) in eastern Laurentia: Implications for global correlation and a

 potential reference section. Geological Magazine, 156, 1311-1322.

Azmy, K., Brand, U., Sylvester, P., Gleeson, S.A., Logan, A., Bitner, M.A., 2011.

 Biogenic and abiogenic low-Mg calcite (bLMC and aLMC): evaluation of

 seawater-REE composition, water masses and carbonate diagenesis. Chem.

 Geol. 280 (1–2), 180-190.

Azmy, K., Kendakk, K., Brand, U., Stouge, S., Gordon, G. W., 2015. Redox

 conditions across the Cambrian-Ordovician boundary: Elemental and isotopic

 signatures retained in the GSSP carbonates . Palaeogeography,

 Palaeoclimatology, Palaeoecology, 440, 440-445.

Barnes, C. R., 1988. The proposed Cambrian-Ordovician global boundary stratotype and point (GSSP) in western Newfoundland, Canada. Geological Magazine, 125, 381-414.

Bau, M., Dulski, p., 1996. Distribution of yttrium and rare-earth elements in the Penge and Kuruman iron-formations, Transvaal Supergroup, South Africa. Precambrian Research, 79, 37-55.

Bian, L., Schovsbo, N.H., Chappaz, A., Zheng, X., Nielsen, A.T., Ulrich, T., Wang, X., Dai, S., Galloway, J.M., Małachowska, A., Xu, X., 2021. Molybdenum uranium-vanadium geochemistry in the lower Paleozoic Alum Shale of Scandinavia: Implications for vanadium exploration. International Journal of Coal Geology, 239, 103730.

Blamey, N.J., Azmy, K., Conliffe, J., 2016. Geochemistry and diagenetic history of the Ordovician Lower Head Formation sandstones, western Newfoundland, Canada. Canadian Journal of Earth Sciences, 53, 1501-1510.

Brand, U., Logan, A., Bitner, M.A., Griesshaber, E., Azmy, K., Buhl, D., 2011. What is the ideal proxy of Paleozoic seawater? Memories Ass. Australasian Palaeontol. Soc. Memories 41, 9–24.

Brasier, M.D., 1982. Sea-level changes, facies changes and the Late Precambrian Early Cambrian evolutionary explosion. Precambrian Research, 17, 105-123.

Brennecka, G. A., Herrmann, A. D., Algeo, T. J., Anbar, A. D., 2011. Rapid expansion of oceanic anoxia immediately before the end-Permian mass

extinction. Proceedings of the National Academy of Sciences, 108, 17631-17634.

Cawood, P. A., McCausland, P. J., Dunning, G. R., 2001. Opening Lapetus: Constraints from Laurentisn Margin in Newfoundland . Geological Society of America Buletin, 113, 443-453.

Çoban-Yıldız, Y., Altabet, M.A., Yılmaz, A. and Tuğrul, S., 2006. Carbon and nitrogen isotopic ratios of suspended particulate organic matter (SPOM) in the Black Sea water column. Deep Sea Research Part II: Topical Studies in Oceanography, 53(17-19), 1875-1892.

Coniglio, M., James, N. P., 1985. Calcified algae as sediment contributors to early Paleozoic limestones; Evidence from deep-water sediments of the Cow Head Group, western Newfoundland. Journal of Sedimentary Research, 55, 746-754.

Coe A. (2003) The Sedimentary Record of Sea-level Change. Cambridge, pp. 287.

Conway, T.M., John, S.G., 2014. The biogeochemical cycling of zinc and zinc isotopes in the North Atlantic Ocean. Global Biogeochemical Cycles, 28, 1111-1128.

Cooper, M.R., Crowley, Q.G., Hollis, S.P., Noble, S.R., Roberts, S., Chew, D., Earls, G., Herrington, R. and Merriman, R.J., 2011. Age constraints and geochemistry of the Ordovician Tyrone Igneous Complex, Northern Ireland: implications for the Grampian orogeny. Journal of the Geological Society, 168, 837-850.

Cooper, R. A., Nowlan, G. S., Williams, S. H., 2001. Global Stratotype Section and point for base of the Ordovician System. Episodes, 24, 19-28.

Cowan, C.A. and James, N.P., 1993. The interactions of sea-level change, terrigenous sediment influx, and carbonate productivity as controls on Upper Cambrian Grand Cycles of western Newfoundland, Canada. Geological Society of America Bulletin, 105, 1576-1590.

Dahl, T.W., Hammarlund, E.U., Anbar, A.D., Bond, D.P., Gill, B.C., Gordon, G.W., Knoll, A.H., Nielsen, A.T., Schovsbo, N.H. and Canfield, D.E., 2010. Devonian rise in atmospheric oxygen correlated to the radiations of terrestrial plants and large predatory fish. Proceedings of the National Academy of Sciences, 107, 17911-17915.

Dickson, J.A.D., 1966. Carbonate identification and genesis as revealed by staining. Journal of Sedimentary Research, 36, 491-505.

Dickson, A. J., Cohen, A. S., 2012. A molybdenum isotope record of Eocene Thermal maximun 2: Implications for global ocean redox during the early Eocene. Paleoceanography, 27, 3230.

Elrick, M., Rieboldt, S., Saltzman, M., Mckay, R. M., 2011. Oxygen-isotope trends and seawater temperature changes across the Late Cambrian Steptoean positive carbon-isotope excursion (SPICE event). Geology, 39, 987-990.

Faure, G., Mensing, T.M., 2005. Principles and applications. John Wiley & Sons, Inc., 897

Fry, B., Jannasch, H.W., Molyneaux, S.J., Wirsen, C.O., Muramoto, J.A. and King, S., 1991. Stable isotope studies of the carbon, nitrogen and sulfur cycles in the Black Sea and the Cariaco Trench. Deep Sea Research Part A. Oceanographic Research Papers, 38, 1003-1019.

German, C.R., Elderfield, H., 1990. Application of the Ce anomaly as a paleoredox indicator: the ground rules. Paleoceanography 5, 823–833.

Gill, B.C., Lyons, T.W., Young, S.A., Kump, L.R., Knoll, A.H., Saltzman, M.R., 2011. Geochemical evidence for widespread euxinia in the Later Cambrian Ocean. Nature, 469, 80-83.

Hibbard, J. P., Van Staal, C. R., Miller, B. V., 2007. Links among Carolinia, Avalonia and Ganderia in the Appalachian peri-Gondwanan realm. Geological society of America Special Papers, 433, 291-311.

Hiscott, R. N., James, N. P., 1985. Carbonate debris flow, Cow Head Group, Western Newfoundland. Journal of Sedimentary Research, 55, 735-745.

Immenhauser, A., Holmden, C., Patterson, W.P., 2008. Interpreting the carbon isotope record of ancient shallow epeiric seas: lessons from the recent. Dynamics of epeiric seas, 48, 137-174.

James, N. P., Mountjoy, W. E., 1983. Shelf-slope break in fossil carbonate platforms: an overview. Special publications of SEPM.

James, N. P., Stevens, R. K., Barnes, C., Knight, I., 1989. Evolution of a Lower Paleozoic continental margin carbonate platform, nothern Canadian

Appalachians. The Society of Economic Paleontologists and Mineralogists, Special Publication, 44.

James, N.P., Stevens, R.K., 1986. Stratigraphy and correlation of the Cambro Ordovician Cow Head Group, western Newfoundland. Geological Survey of Canada.

Johannesson, K.H., Hawkins Jr, D.L., Cortés, A., 2006. Do Archean chemical sediments record ancient seawater rare earth element patterns?. Geochimica et Cosmochimica Acta, 70, 871-890.

Kimura, H., Azmy, K., Yamamuro, M., Zhi-Wen, J., Cizdziel, J. V., 2005. Integrated stratigraphy of the Upper Proterozoic succession in Yunnan of South China: Re-evaluation of global correlation and carbon cycle. Precambrian Research, 138, 1-36.

Kindle, C. H., Whittington, H. B., 1958. Stratigraphy of the Cow Head Region Western Newfoundland. Geological Society of America Bulletin, 69, 315.

Kryc, K.A., Murray, R.W. and Murray, D.W., 2003. Al-to-oxide and Ti-to-organic linkages in biogenic sediment: relationships to paleo-export production and bulk Al/Ti. Earth and Planetary Science letters, 211, 125-141.

Kump, L.R., Junium, C., Arthur, M.A., Brasier, A., Fallick, A., Melezhik, V., Lepland, A., CČrne, A.E. and Luo, G., 2011. Isotopic evidence for massive oxidation of organic matter following the Great Oxidation Event. Science, 334, 1694-1696.

Kunzmann, M., Halverson. G.P., Sossi, P.A., Raub, T.D., Payne, J.L., Kirby, Jason, 2013. Zn isotope evidence for immediate resumption of primary productivity after snowball Earth. Geology 41, 27–30.

Landing, E.D., 2007. Ediacaran–Ordovician of East Laurentia – geologic setting and controls on deposition along the New York Promontory region. In: Landing, E.D. (Ed.), Ediacaran–Ordovician of East Laurentia: S.W. Ford Memorial Volume: New York State Museum Bulletin 510. The University of the State of New York, Albany, New York, 5–24.

Landing, E., Westrop, S.R., Adrain, J.M., 2011. The Lawsonian Stage–the Eoconodontus notchpeakensis (Miller, 1969) FAD and HERB carbon isotope excursion define a globally correlatable terminal Cambrian stage. Bulletin of Geosciences, 86, 621-640.

Landing, E., 2012. Time-specific black mudstones and global hyperwarming on the Cambrian-Ordovician slope and shelf of the Laurentia. Palaeogeography, Palaeoclimatology, Palaeoecology, 367-368, 256-272.

Landing, E., 2013. The great American carbonate Bank in Northeast Laurentia: Its births, deaths, and linkage to continental slope oxygenation (Early Cambrian-Late Ordovician). American Association of Petroleum Geologists Bulletin, Memoir, 98, 451-492.

Landing, E., Geyer, G., Bartowski, K.E., 2002. Latest Early Cambrian small shelly fossils, trilobites, and Hatch Hill dysaerobic interval on the Quebec continental slope. J. Paleontol. 76, 287–305.

Landing, E., Webster, M., 2018, October. Iapetan rift–passive margin transition in NE Laurentia and eustatic control on continental slope oxygenation, Taconic slate colors, and Early Paleozoic climate. In Guidebook to field trips in New York, Vermont, and Massachusetts: 110th New England Intercollegiate Geological Conference and 90th New York Geological Association, Lake George, New York A5-45.

Lavoie, D., Desrochers, A., Dix, G., Knight, I., Hersi, O. S., 2012. The great American carbonate bank in Easter Canada: an Overview. AAPG Special Volumes.

Lawrence, M.G., Greig, A., Collerson, K.D. and Kamber, B.S., 2006. Rare earth element and yttrium variability in South East Queensland waterways. Aquatic Geochemistry, 12, 39-72.

Lerman, A., 1978. Lakes: Chemistry, Geology, Physics. Springer Verlag, Berlin, 57 -60.

Lerman, A., Imboden, D.M. and Gat, J.R. eds., 1995. Physics and chemistry of lakes. Berlin: Springer-Verlag.

Li, D., Zhang, X., Chen, K., Zhang, G., Chen, X., Huang, W., Peng, S., Shen, Y., 2017. High resolution C isotope chemostratigraphy of the uppermost Cambrian stage (stage 10) in South China: Implications for defining the base of stage 10 and palaeoenvironmental change. Geol. Mag. 154, 1232–1243.

Li, D., Zhang, X., Hu, D., Chen, X., Huang, W., Zhang, X., Li, M., Qin, L., Peng, S. and Shen, Y., 2018. Evidence of a large $\delta^{13}C_{carb}$ and $\delta^{13}C_{org}$ depth gradient

for deep-water anoxia during the late Cambrian SPICE event. Geology, 46, 631-634.

Li, D., Zhang, X., Zhang, X., Zhu, H., Peng, S., Sun, L., Shen, Y., 2020. A paired carbonate–organic δ13C approach to understanding the Cambrian Drumian carbon isotope excursion (DICE). Precambrian Research, 349, 105503.

Li, F., Webb, G.E., Algeo, T.J., Kershaw, S., Lu, C., Oehlert, A.M., Gong, Q., Pourmand, A., Tan, X., 2019. Modern carbonate ooids preserve ambient aqueous REE signatures. Chemical Geology, 509, 163-177.

Li, J., Azmy, K., Kendall, B., 2022. The Mo-and U-isotope signatures in alternating shales and carbonate beds of rhythmites: A comparison and implications for redox conditions across the Cambrian-Ordovician boundary. Chemical Geology, 602, 120882.

Liu, X.F., Zhai, S., Wang, X.K., Liu, X. and Liu, X.M., 2022. Rare Earth Element Geochemistry of Late Cenozoic Island Carbonates in the South China Sea. Minerals, 12. 578.

Liyuan, W., Qingjun, G., Changqiu, Z., Rongfei, W., Yinan, D., Xiaokun, H., Liyan, T.,Jing, K., Xi, Y., 2021. Trace and rare earth elements geochemistry of sedimentary rocks in the Ediacaran-Cambrian transition from the Tarim Basin, Northwest China: Constraints for redox environments. Precambrian Research, 352, 105942.

Machel, H.G., Burton, E.A., 1991. Factors governing cathodoluminescence in calcite and dolomite, and their implications for studies of carbonate diagenesis.

Luminescence microscopy and spectroscopy, qualitative and quantitative applications. SEPM Short. Course 25, 37–57.

McLennan, S. B., 1989. Rare earth elements in sedimentary rocks: influence of provenance and sedimentary processes. Mineralogical Society of America, Washington, 169-200.

McLennan, S.M., 2001. Relationships between the trace element composition of sedimentary rocks and upper continental crust. Geochemistry, Geophysics, Geosystems, 2.

Mcllreath, I., James, N., 1978. Facies models 13. Carbonate slopes. Geoscience Canada, 5, 189-199.

Miller, J. F., Evans, K. R., Freeman, R. L., Ripperdan, R. L., Taylor, J. F., 2011. Proposed stratotype for the base of the Lawsonian Stage (Cambrian Stage 10) at the first appearance datum of Econodontus notchpeakensis (Miller) in the house Range, Utah, USA. Bullletin of Geosciences, 86, 595-620.

Morrison, J. O., Brand, U., 1986. Geochemistry of recent marine invertebrates. Geoscience Canada, 13, 237–253.

Neilson, J.E., Brasier, A.T., North, C.P., 2016. Primary aragonite and high-Mg calcite in the late Cambrian (Furongian). Potential evidence from marine carbonates in Oman. Terra. Nova 28, 306–315.

Oehlert, A.M., Swart, P.K., 2014. Interpreting carbonate and organic carbon isotope covariance in the sedimentary record. Nature Communications, 5, 4672.

Pagès, A., Schmid, S., 2016. Euxinia linked to the Cambrian Drumian isotope excursion in Australia: geochemical and chemostratigraphic evidence. Paleo 3 461, 65–76.

Pagès, A., Schmid, S., Edwards, D., Barnes, S., He, N., Grice, K., 2016. A molecular and isotopic study of palaeoenvironmental conditions through the middle Cambrian in the Georgina Basin, central Australia. Earth and Planetary Science Letters, 447, 21-32.

Pattan, J. N., Mir, I. A., Parthiban, G., Karapurkar, S. G., Matta, V. M., Naidu, P. D., Naqvi, S.W. A., 2013. Coupling between suboxic condition in sediments of the western Bay of Bengal and southwest monsoon intensification: A geochemical study. Chemistry Geology, 343, 55–66.

Peng, S., Babcock, L.E., Zhu, X., Zuo, J., Dai, T., 2014. A potential GSSP for the base of the uppermost Cambrian stage, coinciding with the first appearance of Lotagnostus americanus at Wa'ergang, Hunan, China. GFF, 136, 208-213

Pitman Iii, W.C., 1978. Relationship between eustacy and stratigraphic sequences of passive margins. Geological Society of America Bulletin, 89, 1389-1403.

Pulsipher, M. A., Schiffbauer, J. D., Jeffery, M. J., Huntley, J. W., Fike, D. A., Shelton, K. L., 2020. A meta-analysis of the Steptoean Positive Carbon Isotope Excursion: The SPICEraq database. Earth-Science Reviews, 103442.

Quan, T. M., Van de Schootbrugge, B., Field, M., Rosenthal, Y., Falkowski, P. G., 2008. Nitrogen isotope and trace metal analyses from the Mingolsheim core

(Germany): Evidence of redox variations across the Triassic-Jurassic boundary. Global Biogeochem Cycles, 22.

Romaniello, J. S., Herrmann, A. D., Anbar, A. D., 2013. Uranium concentrations and 238U/235U isotope ratios in modern carbonates from the Bahamas: Assessing a novel paleoredox proxy. Chemical Geology, 362, 305-316.

Rush, P.F., Chafetz, H.S., 1990. Fabric retentive, non-luminescent brachiopods as indicators of original δ^{13}C and δ^{18}O compositions: a test. J. Sediment. Petrol. 60, 968–981.

Saltzman, M.R., Ripperdan, R.L., Brasier, M.D., Lohmann, K.C., Robison, R.A., Chang, W.T., Peng, S., Ergaliev, E.K., Runnegar, B., 2000. A global carbon isotope excursion (SPICE) during the Late Cambrian: relation to trilobite extinctions, organic-matter burial and sea level. Palaeogeography, Palaeoclimatology, Palaeoecology, 162, 211-223.

Saltzman, M.R., Runkel, A.C., Cowan, C.A., Runnegar, B., Stewart, M.C., Palmer, A.R., 2004. The upper Cambrian SPICE (δ^{13}C) event and the Sauk II-Sauk III regression: New evidence from Laurentian basins in Utah, Iowa and Newfoundland. Journal of Sedimentary Research 74, 366–377.

Schiffbauer, J. D., Huntley, J. W., Fike, D. A., Jeffery, M. J., Gregg, J. M., Shelton, K. L., 2017. Decoupling biogeochemical records, extinction and environmental change during the Cambrian SPICE event. Science Advances, 3, e1602158.

Schmid, S., 2017. Chemostratigraphy and palaeo-environmental characterisation of the Cambrian stratigraphy in the Amadeus Basin, Australia. Chemical Geology, 451, 169-182.

Shembilu, N., Azmy, K., 2021. Carbon-isotope stratigraphy of the Middle–Upper Cambrian in eastern Laurentia: Implications for global correlation. Marine and Petroleum Geology, 128, 105052.

Shembilu, N. C., Azmy, K., 2022. Trace element variations across Middle–Upper Cambrian carbonates: Implications for the paleoenvironment of eastern Laurentia. Marine and Petroleum Geology, 105385.

Śliwiński, M. G., Whalen, M. T., Day, J., 2010. Trace element variations in the Middle Frasnian Punctata Zone (Late Devonian) in the Western Canada sedimentary basin – Changes in oceanic bioproductivity and paleoredox spurred by a pulse of terrestial afforestation? Geologica Belgica, 4, 459-482.

Stenzel, S. R., Knight, I., James, N. P., 1990. Carbonate platform to foreland basin: revised stratigraphy of the Table Head Group (Middle Ordovician), Western Newfoundland. Canadian Journal of Earthsciences, 27, 14-26.

Swart, P.K., 2015. The geochemistry of carbonate diagenesis: The past, present and future. Sedimentology, 62,1233-1304.

Taylor, S. R., McLennan, S. M., 1985. The continental crust: its composition and evolution.

Terfelt, F., Bagnoli, G., Stouge, S., 2012. Re-evaluation of the conodont lapetognathus and implications for the base of the Ordovician System GSSP. Lethaia, 45, 227-237.

Terfelt, F., Eriksson, M. E., Schmitz, B., 2014. The Cambrian-Ordovician transition in dysoxic facies in Baltica – Diverse faunas and carbon isotope anomalies. Palaeogeography, Palaeoclimatology, Palaeoecology, 394, 59-73.

Tessin, A., Chappaz, A., Hendy, I., Sheldon, N., 2019. Molybdenum speciation as a paleoredox proxy: A case study from Late Cretaceous Western interior seaway black shales. Geology, 47, 59-62.

Tostevin, R., Shields, G.A., Tarbuck, G.M., He, T., Clarkson, M.O. and Wood, R.A., 2016. Effective use of cerium anomalies as a redox proxy in carbonate dominated marine settings. Chemical Geology, 438, 146-162.

Tribovillard, N., Algeo, T. J., Lyons, T., Riboulleau, A., 2006. Trace metals as paleoredox and paleoproductivity proxies:an update. Chem. Geol. 232, 12-32.

Tripathy, G. R., Singh, S. K., Ramaswamy, V., 2014. Major and trace element geochemistry of Bay of Bengal sediments: implications to provenances and their controlling factors. Paleogeography, Paleoclimatology, Paleoecology, 397, 20-30.

Veizer, J., Ala, D., Azmy, K., Bruckschen, P., Buhl, D., Bruhn, F., Carden, G.A., Diener, A., Ebneth, S., Godderis, Y., Jasper, T., 1999. 87Sr/86Sr, δ13C and δ18O evolution of Phanerozoic seawater. Chemical geology, 161, 59-88.

Veizer, J., Compston, W., Clauer, N., Schidlowski, M., 1983. $^{87}Sr/^{86}Sr$ in Late Proterozoic carbonates: evidence for a "mantle" event at ~900 Ma ago. Geochem. Cosmochim. Acta 47 (2), 295–302.

Vindušková, O., Jandová, K., Frouz, J., 2019. Improved method for removing siderite by in situ acidification before elemental and isotope analysis of soil organic carbon. Journal of Plant Nutrition and Soil Science, 182, 82-91.

Voegelin, A., Ralf, K., Jakob, F., Delphine, V., Stephan, J. H., 2010. Effect of phosphate, silica and Ca on Fe (III)-precipitates formed in aerated Fe (II)-and As (III)-containing water studied by X-ray absorption spectroscopy. Geochimica et Cosmochimica Acta, 74, 164-186.

Wang, L., Azmy, K., 2020. Palaeoenvironmental changes in slope carbonates across the Late Cambrian–Early Ordovician in western Newfoundland. Geological Journal, 55, 3451-3463.

Wang, Y., Shi, Z.J., Qing, H.R., Tian, Y.M., Gong, X.X., 2021. Petrological characteristics, geochemical characteristics, and dolomite model of the lower cambrian Longwangmiao Formation in the periphery of the Sichuan Basin, China. Journal of Petroleum Science and Engineering, 202: 108432.

Westrop, S.R., Adrain, J.M., Landing, E., 2011. The Cambrian (Sunwaptan, Furongian) agnostoid arthropod Lotagnostus Whitehouse, 1936, in Laurentian and Avalonian North America: systematics and biostratigraphic significance. Bulletin of Geosciences, 86, 569-594.

Whalen, M. T., Day, J. E., 2008. Magnetic susceptibility, biostratigraphy, and sequence stratigraphy: insights into Devonian carbonate platform development and basin infilling, western Alberta, Canada. Society for Sedimentary Geology, 89, 291-314.

Wignall, P. B., Twitchett, R. J., 1996. Oceanic anoxia and the end Permian mass extinction. Science, 272, 1155-1158.

Wignall, P. B., Zonneveld, J. P., Newton, R. J., Amor, K., Sephton, M. A., Hartley, S., 2007. The end Triassic mass extinction record of Williston Lake, British Columbia. Palaeogeography, Palaeoclimatology, Palaeoecology, 253, 385-406.

Williams, H. R., 1978. The Archaean Geology of Sierra Leone. Precambrian Research, 6, 251-268.

Williams, H., Hiscott, R.N., 1987. Definition of the Iapetus rift-drift transition in western Newfoundland. Geology, 15, 1044-1047.

Wilson, J.L., Medlock, P.L., Fritz, R.D., Canter, K.L., Geesaman, R.G., Candelaria, M.P., Reed, C.L., 1992. A review of Cambro-Ordovician breccias in North America. Paleokarst, karst-related diagenesis and reservoir development. SEPM-Permian Basin Section, Publication, 92, 19-29.

Xia, W., Chen, A., Azmy, K., Sun, S., Li, R., Xu, S., Li, Q., Dong, Y., 2023. A pilot study of upper Yangtze shallow-water carbonates of the Paibian global marine euxinia: Implications for the late Cambrian SPICE event. Marine and Petroleum Geology, 106146. https://doi.org/10.1016/j.marpetgeo.2023.106146

Yang, J.Q., Zhang, J.T., He, Z.L., Zhang, T., 2023. Paleoenvironment reconstruction of the Middle Ordovician thick carbonate from western Ordos Basin, China. Petroleum Science, 20, 48-59.

Yano, M., Yasukawa, K., Nakamura, K., Ikehara, M., Kato, Y., 2020. Geochemical features of redox-sensitive trace metals in sediments under oxygen-depleted marine environments. Minerals, 10, 1021.

Yao, C. Y., Guo, W. M., Liu, J. N., Li, H. W., 2017. Multiple proxies on the paleoenvironment of the Early Cambrian marine black rock series in the Tarim Basin, NW China: Molybdenum isotope and trace element evidence . International Journal of Geosciences, 8, 965-983.

Zhang, P., Wang, Y., Zhang, X., Wei, Z., Wang, G., Zhang, T., Ma, H., Wei, J., He, W., Ma, X., Zhu, C., 2022. Carbon, oxygen and strontium isotopic and elemental characteristics of the Cambrian Longwangmiao Formation in South China: Paleoenvironmental significance and implications for carbon isotope excursions. Gondwana Research, 106, 174-190.

Zhao, R., Mogollón, J.M., Abby, S.S., Schleper, C., Biddle, J.F., Roerdink, D.L., Thorseth, I.H., Jørgensen, S.L., 2020. Geochemical transition zone powering microbial growth in subsurface sediments. Proceedings of the National Academy of Sciences, 117, 32617-32626.

Zhao, Z., Ahlberg, P., Thibault, N., Dahl, T.W., Schovsbo, N.H., Nielsen, A.T., 2022. High-resolution carbon isotope chemostratigraphy of the middle Cambrian to

lowermost Ordovician in southern Scandinavia: Implications for global correlation. Global and Planetary Change, 209, 103751.

Zhao, Z., Thibault, N.R., Dahl, T.W., Schovsbo, N.H., Sørensen, A.L., Rasmussen, C.M., Nielsen, A.T., 2022. Synchronizing rock clocks in the late Cambrian. Nature Communications, 13, 1990.

Appendix 1. Samples, isotopic and elemental compositions of the investigated carbonates (concentrations of elements are in ppm). The $\delta^{13}C_{carb}$ and $\delta^{18}O$ data of the post-SPICE interval are from Azmy (2019b) whereas the entire HERB data (elemental and isotopic geochemistry) are from Wang and Azmy (2020).

Sample id	CaCO₃%	MgCO₃%	$\delta^{13}C_{carb}$ (‰VPDB)	$\delta^{18}O$ (‰VPDB)	$\delta^{13}C_{org}$ (‰VPDB)	TOC wt.%	$\delta^{15}N_{org}$ (Air)	Sr	P	Ni	Cu	Zn	Rb	Cr	Al	Ti	Mn	Fe	U	Th	Y	La	Ce	Pr	Nd	Sm	Eu	Gd	Tb	Dy	Ho	Er	Tm	Yb	Lu	ΣREE
HERB																																					
MH1	98.5	1.5	0.6	-7.1	-30.4	1.43	3.0	687	126	3	7	0.9	2.8	5	1346	38	150	1546	0.4	0.6	4.0	6.0	10.3	1.4	4.9	0.9	0.2	0.6	0.1	0.6	0.1	0.3	0.0	0.2	0.0	26
MH2			0.1	-7.1	-29.5	0.60	3.9																												
MH3	98.6	1.4	-0.7	-7.1	-29.1	0.99		536	183	4	8	1.2	3.2	5	1668	33	335	2478	0.4	0.7	10.0	11.3	20.8	2.2	8.6	1.2	0.3	1.3	0.2	1.2	0.3	0.9	0.1	0.6	0.1	49
MH4			-0.1	-7.6	-29.5	0.54	3.5																												
MH5	98.2	1.8	-0.3	-6.9	-28.6	2.71	3.7	979.8	252	4	9		1.6	5	614	17	253	2747	0.2	0.2	4.8	10.5	13.3	1.8	6.8	1.0	0.2	0.8	0.1	0.6	0.1	0.3	0.0	0.2	0.1	36.0
MH6			-1.1	-7.8	-28.7	0.48																												
MH7	98.5	1.5	-1.9	-7.6	-28.2	0.83	4.0	596	85	4	6	2.0	2.9	5	1785	40	271	4604	0.2	0.6	7.2	12.8	20.6	2.4	9.0	1.4	0.3	1.1	0.2	1.0	0.2	0.6	0.1	0.5	0.1	50
MH8			-1.7	-7.3																														
MH9	98.4	1.6	-1.7	-7.6	-28.0	0.68	3.9	498	123	5	7	3.9	4.4	6	1967	54	339	4932	0.2	0.8	6.9	13.0	21.7	2.7	9.8	1.6	0.3	1.2	0.2	1.0	0.2	0.6	0.1	0.4	0.1	53
MH10			-1.7	-7.5																														
MH11	98.2	1.8	-1.9	-7.8	-28.3	0.64	5.0	233	145	6	7	2.3	4.2	6	2672	57	433	5201	0.4	2.2	11.2	20.9	33.0	3.9	14.8	2.4	0.6	1.9	0.3	1.7	0.4	0.9	0.2	0.7	0.2	82
MH12			-0.7	-7.8	-30.4	0.57	2.7																												
MH13			-1.2	-7.8	-27.8	0.30																												
MH14			-1.3	-7.1																														
MH15	97.9	2.1	-1.4	-7.2			3.7	187	115	5	8	16.8	3.3	6	3202	40	572	6900	0.3	1.2	19.1	24.5	38.8	4.1	15.7	2.3	0.6	2.3	0.4	2.5	0.6	1.5	0.3	1.3	0.3	95.1
MH16			-1.4	-7.3	-29.9	0.85	3.3																												
MH17			-1.1	-7.5																														
MH18	98.9	1.1	-0.6	-7.3	-30.5	1.67		216	128	9	9	3.0	2.5	4	1038	27	387	1326	2.0	0.6	9.6	10.4	19.6	2.2	8.1	1.6	0.3	1.3	0.3	1.4	0.3	0.8	0.1	0.7	0.1	47
MH19	97.2	2.8	-2.1	-7.3	-28.0	0.99	2.9	165	159	4	5	14.4	3.8	5	2400	48	438	3852	1.0	0.9	16.7	17.0	26.6	3.1	12.1	2.0	0.5	1.9	0.3	1.8	0.4	1.1	0.2	0.8	0.1	68
MH20			-1.2	-7.2																														
MH21			-1.1	-7.1	-29.2	0.79																												
MH22			-0.7	-6.9	-28.9	0.88	4.0																												
MH23			-0.7	-7.0																														
MH24	98.9	1.1	-0.6	-7.0	-29.2	1.17		238	113	3	5	0.6	2.2	4	892	28	228	1074	0.9	0.4	5.8	8.2	14.0	1.4	5.9	1.0	0.2	0.8	0.1	0.9	0.2	0.5	0.1	0.4	0.1	34
MH25			-0.7	-7.0	-28.6	0.52	3.2																												
MH26			-0.2	-6.8	-28.5	1.51																												
MH27			-0.8	-7.1	-28.3	0.51																												
MH28			-0.3	-7.2	-29.0	0.93	2.6																												
MH29	98.8	1.2	-1.3	-6.9			0.8	218	142	3	6		2.0	5	1103	43	562	1465	3.6	0.4	17.5	19.1	33.1	3.5	14.5	2.3	0.5	2.2	0.4	2.4	0.5	1.3	0.2	1.2	0.2	81
MH30			-1.1	-7.6																														
MH31			-0.2	-7.2		3.10	2.1																											
MH32	98.7	1.3	0.2	-7.0	-28.7	0.89	1.4	231	94	2	5		1.6	3	833	22	183	1027	1.0	0.2	5.6	7.4	10.3	1.3	4.6	0.8	0.2	0.6	0.1	0.7	0.1	0.3	0.1	0.3	0.0	27
MH33			-0.1	-6.9	-28.3	0.67																												
MP1			-0.9	-7.1	-29.6	0.56																												
MP2	98.8	1.2	-1.5	-7.0	-29.6	0.67		310	86	2	12		1.5	3	820	24	292	1027	0.8	0.1	4.7	7.5	10.6	1.2	4.6	0.6	0.2	0.6	0.1	0.6	0.2	0.3	0.0	0.3	0.0	27
MP3			0.1	-6.8	-29.6	0.98																												
MP4			0.3	-6.8																														
MP5	99.0	1.0	0.6	-6.8	-28.5	2.15		250	150	2	5		1.4	3	681	24	523	904	1.6	0.2	4.7	6.0	9.7	1.1	4.6	0.7	0.2	0.7	0.1	0.6	0.1	0.4	0.1	0.3	0.0	25
MP6			-0.7	-7.1	-29.4	1.11																												
MP7			-0.3	-6.6	-29.5	1.29	2.7																												
MP8	97.3	2.7	-1.1	-7.2	-29.4	0.71	2.3	262	205	4	6	21.7	4.1	7	1992	68	360	2336	2.1	0.6	11.3	15.2	23.6	2.9	11.6	2.1	0.4	1.7	0.2	1.5	0.3	0.8	0.1	0.5	0.1	61
MP9			-0.5	-6.8	-28.2	0.38	2.5																												
MP10	98.9	1.1	0.5	-6.8	-29.6	1.09		247	191	2	6		2.0	7	794	31	569	1019	0.8	0.3	5.1	7.3	11.2	1.4	5.6	0.9	0.2	0.6	0.1	0.7	0.1	0.4	0.1	0.3	0.1	29
MP11			0.2	-6.8	-29.9	1.58																												
MP12			0.3	-7.1	-29.3	1.55																												
MP13			0.8	-6.9																														
MP14	99.0	1.0	1.0	-6.5	-29.6	0.57	2.4	194	116	7	17	1.2	1.9	3	611	32	569	785	2.6	1.5	6.9	9.1	13.7	1.7	6.2	1.1	0.5	1.0	0.3	1.0	0.4	0.7	0.3	0.6	0.3	37
MP15			1.0	-6.4	-29.6	0.80																												

Sample id	CaCO₃%	MgCO₃%	$\delta^{13}C_{carb}$ (‰VPDB)	$\delta^{18}O$ (‰VPDB)	$\delta^{13}C_{org}$ (‰VPDB)	TOC wt.%	$\delta^{15}N_{org}$ (Air)	Sr	P	Ni	Cu	Zn	Rb	Cr	Al	Ti	Mn	Fe	U	Th	Y	La	Ce	Pr	Nd	Sm	Eu	Gd	Tb	Dy	Ho	Er	Tm	Yb	Lu	∑REE
Post-SPICE (NL1 & NL2)																																				
B1-3	96.5	3.5	-1.7	-7.3	-28.7	0.43	3.8	202	139	1.3	0.9	2.7	1.3	1.2	555	85	545	5,017	1.8	0.9	8.6	18.6	28.1	3.1	11.1	1.8	0.4	1.5	0.2	1.5	0.3	0.7	0.1	0.6	0.1	67.9
B2-1	96.4	3.6	-4.3	-7.9	-28.8	0.52	4.4	195	391	2.6	1.2	3.2	1.0	1.5	491	87	511	4,018	0.4	0.5	14.8	35.8	49.8	5.3	19.5	2.7	0.7	2.4	0.4	2.4	0.5	1.1	0.2	0.9	0.1	121.9
B4-1	99.2	0.8	-2.4	-7.1	-28.4	0.24	5.2	175	85	0.3	0.2	2.7	0.5	0.3	186	102	334	755	0.1	0.2	4.2	9.7	17.2	1.6	5.7	0.9	0.2	0.7	0.1	0.7	0.1	0.3	0.0	0.3	0.0	37.7
B6	93.0	7.0	-1.3	-7.6	-26.4	0.20	3.3	282	346	4.7	0.4	3.5	2.3	2.8	1655	92	367	5,770	0.4	3.2	9.6	25.8	48.1	5.6	21.2	3.3	0.7	2.6	0.3	2.0	0.3	0.8	0.1	0.6	0.1	111.6
B8	70.2	29.8	-0.7	-6.0				73	250	2.1	1.0	2.7	1.0	1.6	783	27	266	7,007	0.6	2.6	5.0	7.7	17.2	2.0	8.3	1.5	0.3	1.2	0.2	1.0	0.2	0.4	0.1	0.4	0.1	40.6
B10	99.0	1.0	-0.6	-7.4	-25.6	0.10		161	148	1.0	0.6	4.7	0.6	1.9	568	75	248	590	0.5	0.6	4.3	7.9	15.9	1.6	6.5	0.9	0.2	0.8	0.1	0.8	0.1	0.4	0.1	0.3	0.0	35.8
B12	98.6	1.4	-1.4	-7.5	-28.4	0.28	5.2	181	143	0.9	0.3	1.6	0.3	1.2	238	96	335	851	2.2	0.7	9.8	13.9	25.8	2.3	8.9	1.4	0.3	1.4	0.2	1.3	0.3	0.7	0.1	0.7	0.1	57.5
B14 #2	98.8	1.2	0.0	-7.6	-29.2	0.34		360	80	0.7	0.3	1.6	0.7	1.6	181	102	196	724	0.3	0.4	4.2	14.1	22.6	2.6	9.7	1.4	0.3	1.1	0.1	0.9	0.2	0.4	0.1	0.3	0.0	53.8
B14 #3			-0.7	-7.4	-29.7	0.30	4.2																													
B16 #1			-0.4	-7.6																																
B 16 #3	99.4	0.6	-0.3	-7.9	-29.2	0.18	3.3																													
B18 #1			-0.7	-8.2				121	96	0.9	0.3	0.8	0.4	1.0	114	104	333	783	0.4	0.2	8.2	26.2	42.7	4.7	17.1	2.3	0.6	1.7	0.2	1.6	0.3	0.8	0.1	0.7	0.1	99.2
B19	98.6	1.4	-0.8	-8.0	-25.9	0.17	2.8	195	111	0.7	0.2	0.9	0.5	1.1	249	99	266	1,372	0.3	0.5	8.4	17.7	31.3	3.5	12.9	2.1	0.4	1.6	0.2	1.5	0.3	0.7	0.1	0.6	0.1	72.9
B20 #2	99.0	1.0	-0.5	-7.2				226	168	1.0	0.6	3.1	1.0	1.3	301	98	165	782	0.5	0.6	4.5	9.2	16.0	1.7	6.6	0.9	0.2	0.7	0.1	0.8	0.1	0.3	0.0	0.2	0.0	37.0
B22 #1	99.3	0.7	-0.4	-7.3	-29.4	0.20	3.9	252	38	1.0	0.3	0.5	0.6	0.5	171	101	221	482	0.1	0.2	2.0	4.8	8.6	0.9	3.2	0.5	0.1	0.4	0.1	0.3	0.1	0.1	0.0	0.1	0.0	19.2
B22 #3			-1.1	-8.2																																
B22 #5	92.9	7.1	-1.5	-7.7	-30.0	0.18	1.6	146	138	1.1	0.3	3.7	0.5	1.7	475	79	280	4,798	0.5	0.6	7.2	13.2	22.5	2.3	9.2	1.5	0.3	1.2	0.2	1.1	0.3	0.5	0.1	0.5	0.1	52.9
B23 #2	99.0	1.0	-0.9	-6.9	-31.0	1.46	1.1	160	153	1.1	0.5	1.8	0.9	0.7	432	88	317	977	4.7	0.7	21.8	23.4	45.8	4.1	16.7	2.8	0.7	2.7	0.4	2.9	0.7	1.7	0.3	1.6	0.3	104.0
B23 #3			-1.3	-7.6																																
B23 #6			-1.3	-7.5	-25.3																															
B23 #9	99.4	0.6	-0.4	-7.5	-29.7	1.25	4.8	1,294	61	0.4	0.1	1.5	0.4	0.6	134	101	103	487	1.0	0.2	1.6	3.3	5.9	0.5	2.1	0.3	0.1	0.3	0.0	0.2	0.1	0.1	0.0	0.1	0.0	13.0
B27 #1			-0.6	-7.6																																
B29 #3	98.2	1.8	0.3	-7.3	-32.5	1.76	2.3	590	118	1.5	0.5	1.5	1.1	2.7	618	95	91	1,185	0.4	0.7	5.9	9.6	17.7	1.9	7.3	1.2	0.3	1.1	0.2	0.9	0.2	0.4	0.1	0.4	0.1	41.2
B29 #5			-0.1	-7.6																																
B29 #7	98.9	1.1	-0.8	-7.0	-27.6	0.56	4.8	173	188	1.1	0.4	1.4	1.0	1.5	585	94	176	816	1.3	0.7	9.3	15.1	26.6	2.3	9.1	1.3	0.3	1.3	0.2	1.3	0.3	0.7	0.1	0.7	0.1	59.4
B31 #2			-0.1	-7.9																																
B31 #3			0.3	-8.2																																
B31 #4	98.6	1.4	0.7	-7.0	-29.8	1.09	1.8	275	171	1.5	0.9	1.3	1.7	1.9	566	110	256	1,137	1.2	0.9	10.4	12.8	26.7	2.4	10.4	1.7	0.4	1.6	0.2	1.6	0.3	0.8	0.1	0.6	0.1	59.9
B31 #7			0.0	-7.0	-28.2		3.3																													
B31 #9			0.7	-7.2	-30.7	0.94	2.6																													
B31 #11	99.0	1.0	-0.4	-7.3				206	116	0.7	0.4	1.5	1.0	1.7	832	73	128	608	0.5	0.6	3.9	6.0	13.3	1.2	4.5	0.7	0.2	0.7	0.1	0.6	0.1	0.3	0.1	0.3	0.0	28.0
B32			-0.7	-5.3	-29.0	0.50	2.9																													
B33 #2	98.7	1.3	1.0	-6.7	-30.9	1.52	1.5	290	105	0.5	0.3	0.6	0.4	0.8	207	100	179	397	0.9	0.3	4.5	5.8	11.0	1.2	4.7	0.8	0.2	0.6	0.1	0.6	0.1	0.3	0.0	0.2	0.0	25.8
B35 #1	98.7	1.3	-0.9	-7.0				259	97	0.1	0.0	1.8	0.2	1.1	81	86	172	501	0.8	0.3	8.1	13.3		1.5	5.5	0.9	0.2	0.8	0.1	0.7	0.1	0.4	0.0	0.2	0.0	32.0
B35 #3	98.7	1.3	-1.4	-7.1	-28.6	2.98	-0.7	336	130	0.7	0.3	1.0	0.2	0.6	124	95	257	948	0.7	0.4	8.3	13.8	23.6	2.6	9.8	1.7	0.4	1.3	0.2	1.3	0.3	0.7	0.1	0.5	0.1	56.2
B36a #2	98.6	1.4	-4.8	-7.5	-29.3	0.52	4.2	212	107	0.3	0.1	1.1	0.5	1.5	281	77		792	0.2	0.4	7.0	9.7	17.5	1.9	7.0	1.1	0.3	0.9	0.1	0.9	0.2	0.5	0.1	0.4	0.1	40.7
B36a #3	98.8	1.2	-0.8	-7.6	-30.0	0.51	2.5	205	101	0.5	0.2	2.4	1.0	1.3	517	77	605	1,778	1.6	0.7	22.0	18.2	34.8	3.5	13.9	2.2	0.7	2.3	0.4	2.6	0.6	1.5	0.2	1.2	0.2	82.2
B36a #4			-1.3	-7.6	-29.5	0.53	3.5																													
B36a #5	98.8	1.2	-3.9	-7.6	-30.1	0.78	2.9	189	100	1.1	0.4	1.1	1.6	1.7	674	95	802	1,160	0.4	0.7	9.9	10.8	20.0	2.1	8.5	1.2	0.4	1.1	0.2	1.2	0.2	0.7	0.1	0.6	0.1	47.2
B36a #6	98.7	1.3	-2.7	-7.3				243	249	1.2	0.7	11.2	1.2	1.4	487	90		1300.3	0.5	0.6	11.3	11.9	23.8	2.6	11.0	2.0	0.5	1.8	0.3	1.7	0.3	0.8	0.1	0.7	0.1	57.6
B36c #1	97.3	2.7	-0.1	-7.4	-28.2		3.7	387	97	0.8	0.3	1.9	1.3	1.4	620	81	322	2,627	0.4	0.6	9.1	13.9	23.1	2.5	9.6	1.5	0.4	1.4	0.2	1.2	0.2	0.7	0.1	0.4	0.1	55.3
B36c #2	98.9	1.1	0.6	-7.4	-27.9		1.5	547	137	0.8	0.9	1.5	0.9	1.6	387	89	301	1,262	0.3	0.7	7.1	9.5	18.6	2.0	8.3	1.5	0.3	1.2	0.2	1.1	0.2	0.5	0.1	0.5	0.1	44.1
B36c #4	97.6	2.4	-2.0	-7.3	-29.2	0.44	2.7	561	182	0.6	0.2	0.7	0.5	1.0	316	76	202	1,241	0.4	0.5	11.8	13.0	25.3	2.9	11.3	1.8	0.5	1.7	0.3	1.7	0.3	0.9	0.1	0.6	0.1	60.5
B36d-1	98.8	1.2	-0.7	-7.0				436	104	0.2	0.9	0.4	0.6	0.8	357	84	183	455	0.2	0.3	3.6	4.6	8.6	0.9	3.8	0.6	0.2	0.5	0.1	0.5	0.1	0.3	0.0	0.2	0.0	20.5
B36d-2	98.9	1.1	-1.0	-7.3	-28.9	0.80	4.6	504	144	0.4	5.4	0.9	0.5	0.9	274	94	339	822	0.5	0.3	10.9	9.2	16.9	1.7	7.1	1.2	0.3	1.1	0.2	1.3	0.3	0.8	0.1	0.7	0.1	40.9
B36e	98.5	1.5	-0.4	-7.6	-30.3	1.33	2.3	404	134	0.9	4.9	2.1	0.9	1.8	542	88	240	2,093	1.0	0.7	10.7	13.7	26.3	2.7	10.8	1.8	0.4	1.7	0.2	1.5	0.3	0.7	0.1	0.6	0.1	60.9